

# Comparison of methods for coupled earthquake and tsunami modeling

Lauren S. Abrahams<sup>1</sup>, Lukas Krenz<sup>2</sup>, Eric M. Dunham<sup>1,3</sup>, Alice-Agnes Gabriel<sup>4,5</sup>, and Tatsuhiko Saito<sup>6</sup>

<sup>1</sup>Department of Geophysics, Stanford University, Stanford, CA, USA

<sup>2</sup>Technical University of Munich, Munich, Germany

<sup>3</sup> Institute for Computational and Mathematical Engineering, Stanford University, Stanford, CA, USA

<sup>4</sup>Ludwig-Maximilians-Universität München, Munich, Germany

<sup>5</sup>Scripps Institution of Oceanography, UC San Diego, La Jolla, CA, USA

<sup>6</sup>National Research Institute for Earth Science and Disaster Resilience, Tsukuba, Japan

This manuscript is a non-peer reviewed preprint submitted to EarthArXiv. It is currently in review with Geophysical Journal International - Seismology.

---

Corresponding author: Lauren S. Abrahams, [labraha2@stanford.edu](mailto:labraha2@stanford.edu)

19 **1 Summary**

20 Tsunami generation by offshore earthquakes is a problem of scientific interest and  
21 practical relevance, and one that requires numerical modeling for data interpretation and  
22 hazard assessment. Most numerical models utilize two-step methods with one-way cou-  
23 pling between separate earthquake and tsunami models, based on approximations that  
24 might limit the applicability and accuracy of the resulting solution. In particular, stan-  
25 dard methods focus exclusively on tsunami wave modeling, neglecting larger amplitude  
26 ocean acoustic and seismic waves that are superimposed on tsunami waves in the source  
27 region. In this study, we compare four earthquake-tsunami modeling methods. We iden-  
28 tify dimensionless parameters to quantitatively approximate dominant wave modes in  
29 the earthquake-tsunami source region, highlighting how the method assumptions affect  
30 the results and discuss which methods are appropriate for various applications such as  
31 interpretation of data from offshore instruments in the source region. Most methods cou-  
32 ple a 3D solid Earth model, which provides the seismic wavefield or at least the static  
33 elastic displacements, with a 2D depth-averaged shallow water tsunami model. Assum-  
34 ing the ocean is incompressible and tsunami propagation is negligible over the earthquake  
35 duration leads to the instantaneous source method, which equates the static earthquake  
36 seafloor uplift with the initial tsunami sea surface height. For longer duration earthquakes,  
37 it is appropriate to follow the time-dependent source method, which uses time-dependent  
38 earthquake seafloor velocity as a forcing term in the tsunami mass balance. Neither method  
39 captures ocean acoustic or seismic waves, motivating more advanced methods that cap-  
40 ture the full wavefield. The superposition method of Saito et al. (2019) solves the 3D elas-  
41 tic and acoustic equations to model the seismic wavefield and response of a compress-  
42 ible ocean without gravity. Then, changes in sea surface height from the zero-gravity so-  
43 lution are used as a forcing term in a separate tsunami simulation, typically run with  
44 a shallow water solver. A superposition of the earthquake and tsunami solutions pro-  
45 vides an approximation to the complete wavefield. This method is algorithmically a two-  
46 step method. The complete wavefield is captured in the fully-coupled method, which uti-  
47 lizes a coupled solid Earth and compressible ocean model with gravity (Lotto & Dun-  
48 ham, 2015). The fully-coupled method, recently incorporated into the 3D open-source  
49 code SeisSol, simultaneously solves earthquake rupture, seismic waves, and ocean response  
50 (including gravity). We show that the superposition method emerges as an approxima-  
51 tion to the fully-coupled method subject to often well-justified assumptions. Further-  
52 more, using the fully-coupled method, we examine how the source spectrum and ocean  
53 depth influence the expression of oceanic Rayleigh waves. Understanding the range of  
54 validity of each method, as well as its computational expense, facilitates the selection  
55 of modeling methods for the accurate assessment of earthquake and tsunami hazards and  
56 the interpretation of data from offshore instruments.

57 **Keywords:**

- 58 • Tsunamis
- 59 • Subduction zone processes
- 60 • Mechanics, theory, and modeling
- 61 • Guided waves
- 62 • Wave propagation
- 63 • Computational seismology

## 2 Introduction

Computational modeling coupling the solid Earth and ocean is crucial for studying earthquake-driven tsunami generation. Applications include interpreting data from actual events (Tanioka & Sataka, 1996; Fujii & Satake, 2007; Simons et al., 2011; Yamazaki et al., 2018), informing tsunami early warning (Liu et al., 2009; Bernard & Titov, 2015; Selva et al., 2021), and performing scenario modeling of subduction events (Witter et al., 2013; Hayes et al., 2014; LeVeque et al., 2016; Baba et al., 2016; Goda et al., 2017; Grezio et al., 2017; Scala et al., 2020) and offshore strike-slip events (Ulrich et al., 2019; Krenz et al., 2021; Elbanna et al., 2021; Amlani et al., 2022). Earthquakes excite a rich variety of waves in the solid Earth and ocean, including seismic waves, ocean acoustic waves, and surface gravity waves (tsunamis). The modeling of wave generation and propagation in a compressible ocean with gravity has a long history (Stoneley, 1926; Sells, 1965; Kajiura, 1970; Duffy, 1992; M. Nosov, 1999; Levin et al., 2009), with recent advances focused more on algorithms and workflows for forward models and data inversion in realistically complex geometries. Certain applications focus on just one of these waves, for example, surface gravity waves for tsunami hazard assessment or seismic waves for traditional earthquake source characterization. However, other applications require or at least benefit from the modeling of more than one wave type. For example, joint inversion of seismic and tsunami data provide the best constraints on the rupture process of the 2011 Tohoku-Oki event (Yokota et al., 2011; Lay et al., 2011; Satake et al., 2013; Yamazaki et al., 2018). In particular, tsunami data can place much tighter constraints on the extent of shallow slip than seismic and geodetic data, which is critical for accurate tsunami early warning (Cheung et al., 2022; Mulia et al., 2022). In addition, new offshore instrument networks over earthquake source regions, such as DONET in the Nankai Trough (Kawaguchi et al., 2008) and S-net in the Japan Trench (Yamamoto et al., 2016), have demonstrated that the wavefield is a complex superposition of all of the previously mentioned wave types. Fiber optic technologies offer much promise for densely sampling this complex offshore wavefield (Lindsey et al., 2019; Sladen et al., 2019; Zhan et al., 2021). While filtering approaches can be applied to isolate certain waves (Tsushima et al., 2012; Saito & Tsushima, 2016a), the best constraints on the source will be obtained from models that capture all waves. This has motivated the development of new, coupled solid Earth and ocean modeling methods. Other methods utilize a one-way coupling from the solid Earth to the ocean. Some of these account for the time dependence of the seafloor displacement, while others use the static displacement. All of these methods utilize simplifying assumptions, often providing simpler modeling workflows or more efficient computations. However, these assumptions can limit the applicability of the given method.

The purpose of this study is to examine four modeling methods to assess the consequences of the approximations and the relevance of each method to various features of interest in the wavefield. In this study, we use the Lotto and Dunham (2015) method for fully-coupled earthquake and tsunami modeling, which was recently extended from 2D to 3D by Krenz et al. (2021) through an implementation in the open-source code SeisSol (Dumbser & Käser, 2006; Pelties et al., 2014; Breuer et al., 2015; Uphoff et al., 2017). We present verification tests of the fully-coupled approach against an exact solution. Together with shallow water solvers, the SeisSol implementation provides us simulation capabilities for all four modeling methods. We compare these modeling methods in three ways. First, we focus on the ocean response to a specified seafloor displacement. This is done analytically using seafloor-to-sea surface frequency-domain transfer functions (section 4), which highlight the different wave modes that contribute to the overall wavefield, as well as through time-domain numerical simulations (section 5). Next, we study the more realistic problem of wave generation and propagation from earthquake ruptures using SeisSol dynamic rupture simulations in a coupled ocean-solid Earth model. In addition to comparing the modeling methods for this problem (section 6), we identify and discuss prominent features of the seismic and acoustic wavefield. In particular, we ex-

118 amine how the source spectrum and ocean depth influence the expression of oceanic Rayleigh  
119 waves (section 7).

120 The most widely used method for modeling tsunami generation is equating the final,  
121 or static, vertical seafloor displacement from the earthquake to the initial sea surface  
122 uplift, which serves as the initial condition for a tsunami model. This equivalence  
123 arises from the assumption of a hydrostatic ocean response, which is justified when the  
124 horizontal wavelengths of the seafloor displacement are large compared to ocean depth.  
125 These are the same conditions that justify use of the shallow water model for tsunami  
126 propagation. However, short wavelength seafloor perturbations, particularly in deep water  
127 like that characterizing many subduction zone trench regions, cause a non-hydrostatic  
128 response. Kajiura (1963) has shown how this effectively filters the short wavelength features  
129 of the seafloor displacement from the sea surface response.

130 In addition, using the static seafloor displacement to set initial conditions for the  
131 tsunami model assumes that tsunami propagation is negligible over rupture duration,  
132 a condition that is justified for many earthquakes (Kajiura, 1963; Ward, 2001; Tanioka  
133 & Seno, 2001; Saito & Furumura, 2009). This is the basis for the widely used workflow  
134 of computing seafloor uplift from static elastic solutions for fault slip, such as the solutions  
135 of Okada (1985) for dislocations in a homogeneous elastic half-space. However, for  
136 long-duration tsunami earthquakes, extremely large earthquakes, and underwater landslides,  
137 tsunamis can propagate over distances comparable to or exceeding the horizontal  
138 wavelengths of the seafloor displacement while the seafloor is still deforming. This  
139 has motivated tsunami models with a time-dependent source term describing seafloor  
140 uplift added to the mass balance (Kervella et al., 2007; Saito & Furumura, 2009). Recent  
141 modeling studies have explored the importance of accounting for time-dependent seafloor  
142 displacements for accurate tsunami modeling (Madden et al., 2021).

143 Both of these methods assume that the ocean is incompressible, thereby neglecting  
144 ocean acoustic wave generation and propagation. This assumption is justified when  
145 interpreting data far from the source region because the acoustic waves propagate much  
146 faster than the tsunami, allowing a clear separation of these waves. However, the deployment  
147 of pressure gauges and ocean bottom seismometers in the offshore region above or  
148 adjacent to earthquake sources has shown the superposition of tsunami waves, seismic  
149 waves, and ocean acoustic waves (M. Nosov & Kolesov, 2007; Matsumoto et al., 2017;  
150 Saito et al., 2019; Kubota et al., 2021). This has motivated the development of new methods  
151 that aim to capture the full wavefield. We note that several fully-coupled modeling  
152 methods were developed decades ago in the context of mode summation for plane-layered  
153 or spherically symmetric Earth models with a compressible ocean subject to gravity (Ward,  
154 1980, 1981; Comer, 1984; Dahlen & Tromp, 1999). In comparison, the new methods we  
155 focus on here have arisen independently as extensions of 2D and 3D seismic wave propagation  
156 (and in some cases earthquake dynamic rupture) codes that can handle the material  
157 heterogeneity and complex seafloor bathymetry existing in real subduction zones.

158 Maeda and Furumura (2013) were the first to introduce a fully-coupled modeling  
159 method by adding gravity to their seismic and acoustic wave propagation code for solid  
160 Earth and the ocean. Lotto and Dunham (2015) provided an alternative framework for  
161 fully-coupled modeling, starting from the linearized governing equations for small perturbations  
162 of a compressible ocean about an initial hydrostatic rest state. They implemented this model  
163 in a 2D finite difference code for both kinematic and dynamic earthquake ruptures (Lotto &  
164 Dunham, 2015; Lotto et al., 2017, 2018). This method was also successfully implemented  
165 in a 2D finite element code (Wilson & Ma, 2021). The methods of both Maeda and Furumura  
166 (2013) and Lotto and Dunham (2015) simultaneously model all waves in one simulation.  
167 We note that the governing equations of Maeda and Furumura (2013) differ from those of  
168 Lotto and Dunham (2015); the former appear not to have received continued use in the  
169 literature so they will not be explored in our study.

170 In contrast to the fully-coupled modeling methods, Saito et al. (2019) have intro-  
171 duced a two-step sequential modeling method for the same problem. First, the earth-  
172 quake rupture, seismic waves, and ocean acoustic waves are modeled in a coupled Earth  
173 and compressible ocean model without gravity. The sea surface vertical velocity from  
174 this model is then used as a source term in an incompressible 2D tsunami simulation,  
175 using some form of a shallow water solver (e.g., nondispersive linear long wave or weakly  
176 dispersive Boussinesq). The appropriate superposition of the earthquake and tsunami  
177 solutions provides an approximation to the complete wavefield. (For fields other than  
178 the sea surface displacement, this requires computing the 3D ocean response from 2D  
179 shallow water solution, using the assumptions that provide the basis of the depth-integrated  
180 shallow water model.) Even though the tsunami simulation utilizes an incompressible  
181 ocean, this superposition of the earthquake and tsunami solutions accounts for acous-  
182 tic and seismic waves.

183 The fully-coupled and superposition methods require wave propagation simulations  
184 which are computationally expensive and usually require parallel computing in 3D. The  
185 superposition method additionally uses a tsunami simulation to incorporate gravity. This  
186 tsunami simulation is 2D depth-integrated and, for most shallow water models, allows  
187 much larger time steps. Hence it has a vastly smaller computational cost than the ini-  
188 tial 3D simulation. Comparing the fully-coupled and superposition methods, the addi-  
189 tion of gravity adds negligible computational cost. Hence, the superposition method has  
190 no real computational advantage over the fully-coupled method in modeling the wave  
191 generation process. The superposition method offers two possible advantages over the  
192 fully coupled method. First, it can be performed using many existing wave propagation  
193 codes without needing to introduce a stable and accurate treatment of the free surface  
194 boundary condition to account for gravity. Second, it is straightforward to continue run-  
195 ning the efficient tsunami simulation for a much longer time than the initial 3D wave prop-  
196 agation model to study regional or global tsunami propagation as well as inundation (if  
197 a nonlinear tsunami model is used). Currently, there is no established workflow for tran-  
198 sitioning between the fully-coupled method solution and a shallow water tsunami sim-  
199 ulation.

200 In this study, we formally establish the relation between the superposition-based  
201 method of Saito et al. (2019) and the fully-coupled method of Lotto and Dunham (2015),  
202 showing that their differences are negligibly small in many relevant cases. In addition,  
203 we perform verification tests of the recent 3D implementation by (Krenz et al., 2021) of  
204 the Lotto and Dunham (2015) method to 3D in the open-source SeisSol code (Dumbser  
205 & Käser, 2006; Breuer et al., 2015; Pelties et al., 2014; Uphoff et al., 2017). We then use  
206 the fully-coupled SeisSol solution as a reference solution for comparison to alternative  
207 modeling methods. Specifically, we compare results of four modeling methods for a vari-  
208 ety of imposed seafloor displacement and earthquake rupture sources. We explore how  
209 the wavefield is influenced by the horizontal wavelengths characterizing the source, the  
210 source duration, and ocean compressibility. Non-dimensional parameters allow us to quan-  
211 tify the validity of the model assumptions. A comparison of the results reveals discrep-  
212 ancies between the models whenever these assumptions are violated. Understanding the  
213 range of validity of each method, as well as its computational expense, facilitates the se-  
214 lection of modeling method for accurate assessment of earthquake and tsunami hazards  
215 and the interpretation of data from offshore instruments.

216 Our earthquake rupture simulations reveal a complex set of ocean acoustic and seis-  
217 mic waves, the most prominent of which we identify as oceanic Rayleigh waves. We ex-  
218 amine the dispersion properties of these waves to explain key features of the resulting  
219 wavefield, highlighting how the wavefield changes with ocean depth and the frequency  
220 band of waves excited by the earthquake source. We anticipate these results to guide in-  
221 terpretation of data from offshore instruments.

### 3 Methods for Coupled Earthquake-Tsunami Modeling

This section outlines the four modeling methods used in this study. Starting with the general problem, we derive the fully-coupled method (method 1). Next, we apply approximations to the general problem to derive commonly used shallow water methods (methods 2 and 3) and the recently developed superposition method (method 4). The methods are summarized in Fig. 1. Method 2 assumes an incompressible ocean and that tsunami propagation is negligible over the duration of the earthquake, so that tsunami generation is captured by specifying initial sea surface height in the tsunami model. Often the initial sea surface height is equated to the static seafloor uplift from an earthquake model. In some applications of this method, the seafloor uplift is filtered to remove short wavelength components when translating to initial sea surface height; the filter, referred to as the Kajiura filter, is based on an analytic solution to Laplace's equation for pressure (or velocity potential) in an incompressible ocean of uniform depth and accounts for non-hydrostatic response at short wavelengths (Kajiura, 1963, 1970; Tanioka & Satake, 1996). For longer-duration earthquakes, it is more appropriate to follow method 3, which uses the time-dependent seafloor velocity from an earthquake model as a time-dependent forcing term in the tsunami mass balance equation (Saito & Furumura, 2009; Saito & Tsushima, 2016b; Saito, 2019).

We remark that the shallow water solver used in these two methods can solve either linearized equations, if attention is restricted to the offshore region, or nonlinear equations, for applications involving inundation and run-up and other problems where nonlinearities are important. In this study, we limit our attention to the offshore region where the linear shallow water equations are justified. In addition, the effects of dispersion on tsunami propagation can be accounted for approximately with a Boussinesq solver or neglected in the more commonly used linear long wave model.

Neither method 2 nor method 3 captures ocean acoustic or seismic waves, motivating the development of more advanced methods. Saito et al. (2019) propose a superposition-based modeling method, referred to here as method 4, which solves the 3D elastic and acoustic wave equations to model the earthquake rupture, seismic wavefield, and the response of a compressible ocean without gravity. Then, changes in sea surface height from this zero-gravity solution are used as a time-dependent forcing term in a separate, shallow water tsunami simulation. A superposition of the earthquake and tsunami solutions provides the complete wavefield, with some approximations applied to the tsunami propagation problem depending on the shallow water solver used (linear long wave or Boussinesq). Thus, while method 4 is algorithmically a two-step method, like methods 2 and 3, it provides more than just the tsunami wavefield. The complete wavefield is captured in method 1, which directly solves the equations governing the response of a fully-coupled solid Earth and ocean with gravity (Lotto & Dunham, 2015).

#### 3.1 Statement of the general problem

Consider perturbations to an ocean of equilibrium depth  $H(x, y)$ . The  $z$ -axis is vertical and directed upward, opposite to gravity and the unperturbed sea surface is the plane  $z = 0$ . We use an Eulerian description. We consider first problems in which the seafloor displacement is specified, then replace this with acoustic-elastic interface conditions at the seafloor to couple the ocean to the solid Earth. For the first class of problems, an earthquake, or another source, causes vertical uplift  $b(x, y, t)$  of the seafloor, such that the seafloor is now located at  $z = -H(x, y) + b(x, y, t)$ . The vertical uplift has contributions from both vertical and horizontal displacements ( $U_i$ ) of the solid Earth if the seafloor is sloped. Tanioka and Satake (1996) introduced the widely used linearized relation,

$$b = U_z + U_x \frac{\partial H}{\partial x} + U_y \frac{\partial H}{\partial y}, \quad (1)$$

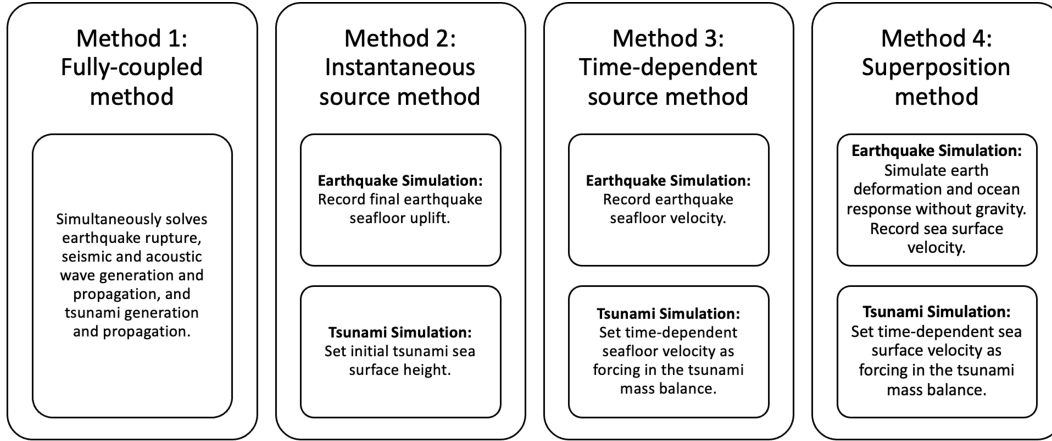


**Figure 1.** We compare four modeling methods in this paper. Method 1, the fully-coupled method, simultaneously solves earthquake rupture and ocean response. Methods 2-4 are two-step methods, using approximations to send information from an earthquake simulation into a separate tsunami simulation. Only methods 1 and 4 capture the full wavefield; methods 2 and 3 are limited to tsunami waves.

261  
262

which is valid when deformation-induced changes in bathymetry are sufficiently small. The perturbed ocean surface is  $z = \eta(x, y, t)$ .

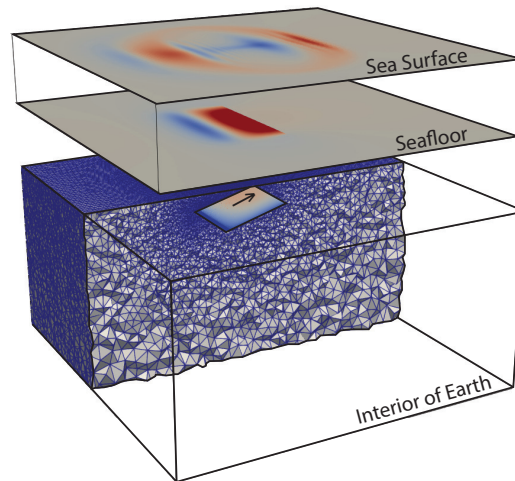


**Figure 2.** 3D model domain with an underlying elastic solid and overlying acoustic ocean. The full domain is discretized with an unstructured tetrahedral mesh. Surfaces offset for visualization.

In this general problem, the ocean is compressible and inviscid, with gravity acting as a restoring force. Following Lotto and Dunham (2015), the governing equations for small perturbations about an initial hydrostatic equilibrium rest state of the ocean are derived by combining the mass balance (continuity) with a linearized equation of state, yielding

$$\frac{1}{K} \frac{\partial p}{\partial t} + \frac{\partial v_x}{\partial x} + \frac{\partial v_y}{\partial y} + \frac{\partial v_z}{\partial z} = 0, \quad (2)$$

and the momentum balance equations,

$$\rho \frac{\partial v_x}{\partial t} + \frac{\partial p}{\partial x} = 0, \quad (3)$$

$$\rho \frac{\partial v_y}{\partial t} + \frac{\partial p}{\partial y} = 0, \quad (4)$$

and

$$\rho \frac{\partial v_z}{\partial t} + \frac{\partial p}{\partial z} = 0, \quad (5)$$

263 for particle velocities  $v_i$ , pressure perturbation  $p$ , bulk modulus  $K$ , and density  $\rho$ . The  
 264 sound speed is  $c_0 = \sqrt{K/\rho}$ . We neglect source terms of  $\mathcal{O}(g/\omega c_0)$ , where  $\omega$  is the an-  
 265 gular frequency characterizing a wave and  $g$  is the gravitational acceleration (Lotto &  
 266 Dunham, 2015). The governing equations, as written, can have depth-dependent  $\rho$  and  
 267  $K$ . Accounting for this depth dependence is necessary for a rigorous inclusion of com-  
 268 pressibility effects using a linearized equation of state. Instead, we assume in this study  
 269 that both  $\rho$  and  $K$  are constants which incurs an error of  $\mathcal{O}(gH/c_0^2)$  which is quite small  
 270 for Earth's oceans and can thus be neglected.

With these approximations, gravity enters only through a linearization of the free surface boundary condition,

$$p - \rho g \eta = 0, \quad \text{at } z = 0. \quad (6)$$

The equations are closed by adding the linearized kinematic condition on the sea surface,

$$\frac{\partial \eta}{\partial t} = v_z, \quad \text{at } z = 0, \quad (7)$$

and, for problems in which the seafloor displacement is specified, the linearized kinematic condition on the seafloor,

$$\frac{\partial b}{\partial t} = v_z + v_x \frac{\partial H}{\partial x} + v_y \frac{\partial H}{\partial y}, \quad \text{at } z = -H. \quad (8)$$

271 Note that (1) follows directly from time integration of (8). For problems that couple the  
 272 ocean to the solid Earth, the seafloor kinematic condition is replaced with the follow-  
 273 ing acoustic-elastic interface conditions at the seafloor: 1) continuity of normal displace-  
 274 ment, 2) balancing normal traction on the solid side with pressure on the ocean side, 3)  
 275 vanishing shear traction on the solid side.

### 276 **3.2 Method 1: Fully-coupled method**

277 The fully-coupled method, which provides a reference solution to which solutions  
 278 from other methods are compared, is obtained by solving equations (2)-(7) in the ocean  
 279 and the elastic wave equation in the solid Earth. The ocean and solid are coupled by en-  
 280 forcing continuity of the normal velocity and traction components of stress across the  
 281 seafloor interface, rather than imposing the seafloor uplift through the kinematic con-  
 282 dition (8).



283  
284

### 3.3 Approximations to method 1 (fully-coupled method) yield shallow water modeling methods 2 and 3

285  
286  
287  
288  
289  
290

The most commonly used methods for modeling tsunami generation and propagation couple a 3D Earth model with a 2D depth-averaged shallow water tsunami model. Starting with the general problem governed by equations (2)-(8), we make two well-known approximations to obtain the linearized shallow water equations. First, when  $\omega H/c_0 \ll 1$ , where  $\omega$  is the angular frequency, the ocean responds in an effectively incompressible manner. This eliminates the  $K^{-1}\partial p/\partial t$  term in (2).

We then depth integrate the resulting continuity equation for an incompressible fluid and use the linearized kinematic conditions (7) and (8) to obtain

$$\frac{\partial \eta}{\partial t} + \frac{\partial q_x}{\partial x} + \frac{\partial q_y}{\partial y} = \frac{\partial b}{\partial t}, \quad (9)$$

in which the linearized depth-integrated horizontal velocities, also know as fluxes, are

$$q_x = \int_{-H}^0 v_x dz, \quad q_y = \int_{-H}^0 v_y dz. \quad (10)$$

Second, we neglect the inertial term  $\rho \partial v_z / \partial t$  in the vertical momentum balance (5), such that the pressure perturbation  $p$  is independent of depth and equal to the hydrostatic pressure change  $\rho g \eta$ . This is justified when vertical accelerations are small compared to  $g$ , which occurs for small-amplitude perturbations when  $kH \ll 1$ , where  $k$  is the horizontal wavenumber characterizing the solution. It then follows from (6) that the horizontal pressure gradient is independent of depth. Thus, the horizontal momentum balances (3) and (4) become independent of depth, and after depth integration are

$$\frac{\partial q_x}{\partial t} + gH \frac{\partial \eta}{\partial x} = 0 \quad (11)$$

and

$$\frac{\partial q_y}{\partial t} + gH \frac{\partial \eta}{\partial y} = 0. \quad (12)$$

291  
292  
293

Equations (9), (11), and (12) are the linear long wave equations that describe nondispersive tsunami propagation at the shallow water wave speed  $(gH)^{1/2}$ . These are the equations used in most parts of this study for the shallow water problem.

We remark that effects of dispersion can be approximately accounted for using the Boussinesq approximation (Saito et al., 2010; Baba et al., 2015, 2017; Saito, 2019), which adds non-hydrostatic pressure correction terms to the momentum balances (11) and (12):

$$\frac{\partial q_x}{\partial t} + gH \frac{\partial \eta}{\partial x} = \frac{1}{3} H^2 \frac{\partial^2}{\partial x \partial t} \left( \frac{\partial q_x}{\partial x} + \frac{\partial q_y}{\partial y} \right) \quad (13)$$

and

$$\frac{\partial q_y}{\partial t} + gH \frac{\partial \eta}{\partial y} = \frac{1}{3} H^2 \frac{\partial^2}{\partial y \partial t} \left( \frac{\partial q_x}{\partial x} + \frac{\partial q_y}{\partial y} \right). \quad (14)$$

294  
295

We use this Boussinesq model in the final part of our study and compare results to those of the linear long wave model.

296

#### 3.3.1 Method 2: Instantaneous source method

297  
298  
299  
300  
301

Method 2 is the simplest and most commonly used two-step method. It is based on the premise that the earthquake source occurs over such short time scales, as compared to tsunami propagation time scales, that the source can be regarded as instantaneous. In this method, an earthquake model is used to provide the static seafloor uplift  $b_{st}(x, y)$ . This is often computed using dislocation solutions for a uniform elastic half-

302 space, but can also be obtained using the final displacements from a time-dependent kine-  
 303 matic or dynamic rupture simulation. These solutions are typically calculated by neglect-  
 304 ing the ocean and by treating the seafloor as a free surface.

Next, a shallow water tsunami simulation is performed by solving equations (9), (11), and (12), with the forcing term  $\partial b/\partial t$  in (9) set to zero and

$$\eta(x, y, 0^+) = b_{st}(x, y), \quad (15)$$

$$q_x(x, y, 0^+) = 0, \quad (16)$$

$$q_y(x, y, 0^+) = 0, \quad (17)$$

as initial condition. Here,  $t = 0^+$  corresponds to the end of the earthquake and the start of tsunami propagation. The first initial condition (15) follows from the time integration of (9) over the earthquake source region, assuming a dominant balance between sea surface uplift rate  $\partial\eta/\partial t$  and seafloor uplift rate  $\partial b/\partial t$ . This is justified when the seafloor displacement occurs over a sufficiently short time scale such that horizontal fluxes are negligible over the earthquake duration, or equivalently when the tsunami propagation distance over the earthquake duration is much shorter than the horizontal wavelengths characterizing the seafloor uplift. Alternatively, one can view the seafloor uplift forcing, at the much longer time scales of the tsunami, as effectively instantaneous by writing

$$\partial b/\partial t \approx b_{st}(x, y)\delta(t); \quad (18)$$

305 then integrating (9) with this forcing across  $t = 0$  yields the initial condition (15).

306 Setting initial horizontal fluxes to zero (equations 16 and 17) is justified when the  
 307 seafloor displacement transfers negligible horizontal momentum, in the form of tsunami  
 308 waves, to the ocean. While some studies have argued that horizontal momentum trans-  
 309 fer may be important (Song et al., 2008; Song & Han, 2011; Song et al., 2017), simula-  
 310 tions using a 2D fully-coupled model (Lotto et al., 2017, 2018) show that it is negligi-  
 311 ble for the geometries and problems of interest here.

312 We note that there are variants of method 2 in which  $b_{st}(x, y)$  is filtered to account  
 313 for non-hydrostatic effects at short wavelengths during the tsunami generation process  
 314 prior to setting the initial condition on  $\eta(x, y, 0^+)$  (Kajiura, 1963, 1970; M. A. Nosov &  
 315 Kolesov, 2011). This is often referred to as the Kajiura filter. Likewise, the tsunami prob-  
 316 lem can be solved using a nonlinear shallow water solver and/or a Boussinesq solver that  
 317 accounts approximately for tsunami dispersion (Baba et al., 2015, 2017; Saito, 2019; Saito  
 318 & Kubota, 2020).

319 To summarize, this one-way coupled method assumes that the ocean is incompress-  
 320 ible, horizontal wavelengths are much longer compared to ocean depth, and tsunami prop-  
 321 agation is negligible over the earthquake duration.

### 322 **3.3.2 Method 3: Time-dependent source method**

323 For longer duration sources, horizontal flux terms in the tsunami mass balance are  
 324 not negligible while the seafloor is actively deforming, and thus, tsunami propagation  
 325 occurs over the earthquake duration. In this case, the time-dependent forcing term in  
 326 the mass balance must be used when solving the tsunami problem. Similar to method  
 327 2, an earthquake simulation computes  $b(x, y, t)$ . It is insufficient to only compute the static  
 328 uplift,  $b_{st}(x, y)$ . The tsunami solution is obtained by solving the shallow water equations  
 329 (9)-(12) with homogeneous initial conditions. Coupling from the earthquake to the tsunami  
 330 occurs through the forcing term  $\partial b/\partial t$  in the mass balance (9). No forcing is added to  
 331 the momentum balance equations, consistent with the previously stated assumption of  
 332 negligible horizontal momentum transfer from the solid Earth to the ocean during seafloor

333 displacement. Note that method 2 is a limiting case of method 3 for sufficiently short  
 334 duration  $\partial b/\partial t$ .

335 The instantaneous source two-step method (method 2) and time-dependent source  
 336 two-step method (method 3) are generally acceptable for modeling tsunami propagation  
 337 and are prevalent in current modeling practices. However, they do not include contri-  
 338 butions from acoustic waves and cannot be used for certain applications, for example,  
 339 for improving tsunami early warning approaches. For this purpose, we need models that  
 340 capture both acoustic and tsunami waves in the ocean.

### 341 **3.4 Approximations to method 1 (fully-coupled method) yields method** 342 **4 (superposition method)**

343 The fully-coupled method (method 1) provides the full seismic, acoustic, and tsunami  
 344 wavefield. However, this requires a stable and accurate implementation of the free sur-  
 345 face boundary condition with gravity, namely equations 6 and 7, rather than the usual  
 346  $p = 0$  free surface condition that is enforced in most 3D seismic/acoustic wave prop-  
 347 agation codes. Code modifications can be avoided using a superposition-based method  
 348 for computing the full wavefield (Saito, 2019; Saito et al., 2019). We refer to this super-  
 349 position method as method 4. Here we show how the superposition method can be ob-  
 350 tained from the fully-coupled method by making a few approximations that are often  
 351 well-justified; this connection has not previously been recognized in the literature. The  
 352 superposition method differs from the fully-coupled method in that it is algorithmically  
 353 a two-step method that must be implemented using two separate codes, a seismic wave  
 354 propagation code without gravity and a tsunami code. The method passes information  
 355 from an initial zero-gravity simulation, conducted with a compressible ocean and thus  
 356 resolving both acoustic and seismic waves, to a tsunami simulation (which, thus far in  
 357 the literature, has been conducted using incompressible shallow water solvers). The zero-  
 358 gravity simulation provides a time-dependent forcing term for the tsunami simulation,  
 359 and an appropriate superposition of the two solutions provides the full wavefield (Saito,  
 360 2019; Saito et al., 2019).

361 Here we provide a derivation of the superposition method that reduces to the method  
 362 introduced by Saito et al. (2019). We denote by a superscript (1) the zero-gravity so-  
 363 lution obtained by solving governing equations (2)-(5) with boundary conditions (6)-(8),  
 364 but with  $g = 0$  in (6). We denote by a superscript (2) the solution to a second prob-  
 365 lem that when superimposed with solution 1 yields the exact solution to the fully-coupled  
 366 problem. Thus, the superposition of solutions 1 and 2 provides the full wavefield, which  
 367 is, by construction, identical to the fully-coupled solution.

368 We next derive the equations and boundary conditions for solution 2. To do this,  
 369 we write each field as a superposition of the fields from solutions 1 and 2, e.g.,  $p = p^{(1)} +$   
 370  $p^{(2)}$ . Then we subtract the solution 1 governing equations and boundary conditions from  
 371 those for the full solution (which are identical except for the  $\rho g \eta$  term in the top bound-  
 372 ary condition). This procedure yields the solution 2 governing equations

$$\frac{1}{K} \frac{\partial p^{(2)}}{\partial t} + \frac{\partial v_x^{(2)}}{\partial x} + \frac{\partial v_y^{(2)}}{\partial y} + \frac{\partial v_z^{(2)}}{\partial z} = 0, \quad (19)$$

$$\rho \frac{\partial v_x^{(2)}}{\partial t} + \frac{\partial p^{(2)}}{\partial x} = 0, \quad (20)$$

$$\rho \frac{\partial v_y^{(2)}}{\partial t} + \frac{\partial p^{(2)}}{\partial y} = 0, \quad (21)$$

$$\rho \frac{\partial v_z^{(2)}}{\partial t} + \frac{\partial p^{(2)}}{\partial z} = 0, \quad (22)$$

373 and boundary conditions

$$p^{(2)} - \rho g \eta^{(2)} = \rho g \eta^{(1)}, \quad z = 0, \quad (23)$$

$$\frac{\partial \eta^{(2)}}{\partial t} - v_z^{(2)} = 0, \quad z = 0, \quad (24)$$

$$v_z^{(2)} + v_x^{(2)} \frac{\partial H}{\partial x} + v_y^{(2)} \frac{\partial H}{\partial y} = 0, \quad z = -H. \quad (25)$$

374 Note that solution 2 is forced by the  $\rho g \eta^{(1)}$  term in the top boundary condition (23), and  
375 there is no seafloor forcing in (25), as that has been accounted for in solution 1.

376 Thus far, no approximations have been made, and solving for solution 2 requires  
377 exactly the same solver (and involves approximately the same computational cost) as  
378 solving the fully-coupled problem, including the gravity-related term in (23). It is only  
379 by introducing approximations that the superposition method can be performed with  
380 minimal additional computational expense as compared to the fully-coupled method. The  
381 approximations are motivated by the anticipation that solution 2 will be dominated by  
382 tsunami waves, with the remainder being (ideally negligible) corrections to the seismic  
383 and ocean acoustic waves in solution 1. To examine this, we apply the previously described  
384 set of shallow water approximations (incompressibility and depth-independent hydro-  
385 static pressure changes) to the governing equation of solution 2. We denote the approx-  
386 imate solution 2 with a superscript (2'), which can be obtained with a shallow water solver.

387 With these approximations, solution 2' is determined by the linear long wave equa-  
388 tions

$$\frac{\partial \eta^{(2')}}{\partial t} + \frac{\partial q_x^{(2')}}{\partial x} + \frac{\partial q_y^{(2')}}{\partial y} = 0, \quad (26)$$

$$\frac{\partial q_x^{(2')}}{\partial t} + gH \frac{\partial \eta^{(2')}}{\partial x} = -gH \frac{\partial \eta^{(1)}}{\partial x}, \quad (27)$$

$$\frac{\partial q_y^{(2')}}{\partial t} + gH \frac{\partial \eta^{(2')}}{\partial y} = -gH \frac{\partial \eta^{(1)}}{\partial y}. \quad (28)$$

The forcing from solution 1 appears in the momentum balance equations, rather than  
in the mass balance as might have been expected. However, by introducing the (approx-  
imate) total sea surface uplift,

$$\eta' = \eta^{(1)} + \eta^{(2')}, \quad (29)$$

389 and eliminating  $\eta^{(2')}$  in favor of  $\eta'$ , we can replace these equations with

$$\frac{\partial \eta'}{\partial t} + \frac{\partial q_x^{(2')}}{\partial x} + \frac{\partial q_y^{(2')}}{\partial y} = \frac{\partial \eta^{(1)}}{\partial t}, \quad (30)$$

$$\frac{\partial q_x^{(2')}}{\partial t} + gH \frac{\partial \eta'}{\partial x} = 0, \quad (31)$$

$$\frac{\partial q_y^{(2')}}{\partial t} + gH \frac{\partial \eta'}{\partial y} = 0. \quad (32)$$

390 This formulation matches the one introduced by Saito et al. (2019). The forcing has now  
391 been transferred to the mass balance, similar to the tsunami problem in the one-way cou-  
392 pled methods 2 and 3.

393 Finally, we note that the Boussinesq correction terms can be added to the horizon-  
394 tal momentum balances (31) and (32) to account for dispersion during tsunami prop-  
395 agation. Regardless of the choice of shallow water solver, nonhydrostatic effects during  
396 tsunami generation are naturally accounted for in solution 1, by virtue of solving for the  
397 ocean response using a depth-resolved solver. This is similar to, but potentially supe-

398 prior to, the use of a Kajiura filter in that solution 1 accounts for the nonhydrostatic re-  
 399 sponse of a variable depth ocean, whereas the Kajiura filter assumes a uniform depth  
 400 ocean.

### 401 3.5 Implementation of the methods

402 This section explains how the four methods introduced above are implemented and  
 403 utilized in our study. We use the 3D dynamic rupture and wave propagation code Seis-  
 404 Sol, which solves the elastic and acoustic wave equations in velocity-stress formulation  
 405 using the arbitrary high-order derivative Discontinuous Galerkin (ADER-DG) method,  
 406 with kinematic or dynamic rupture sources (Dumbser & Käser, 2006; Pelties et al., 2014;  
 407 Uphoff et al., 2017; Krenz et al., 2021). See Appendix A for verification of this new bound-  
 408 ary condition and Krenz et al. (2021) for discussion of high performance computing as-  
 409 pects of the implementation. We use SeisSol with gravity to provide the method 1 so-  
 410 lution, and an otherwise identical solution without gravity to provide the static or time-  
 411 dependent forcing for methods 2-4. For the shallow water model in methods 2-4, we solve  
 412 the nondispersive linear long wave equations using the code FDMAP (Dunham et al.,  
 413 2011; Kozdon et al., 2012, 2013). While FDMAP was written for 2D antiplane shear and  
 414 plane strain elastodynamic problems, the linear long wave equations are mathematically  
 415 equivalent to the 2D antiplane shear wave equation. In one example at the end of our  
 416 study (section 7.2), we use a Boussinesq solver that accounts for weak dispersion dur-  
 417 ing tsunami propagation (Saito et al., 2010; Saito, 2019).

## 418 4 Seafloor to sea surface transfer functions and wave modes in a uni- 419 form depth ocean

Having presented the four methods, we now compare them. One way to do this is  
 to examine the sea surface response  $\eta(x, y, t)$  to an imposed seafloor uplift  $b(x, y, t)$ . For  
 a uniform depth ocean (i.e., constant  $H$ ), this can be quantified in terms of the Fourier  
 domain transfer function

$$T(k, \omega) = \frac{\hat{\eta}(k_x, k_y, \omega)}{\hat{b}(k_x, k_y, \omega)}, \quad (33)$$

420 for horizontal wavenumbers  $k_x$  and  $k_y$  and angular frequency  $\omega$ , using the convention

$$\hat{f}(k_x, k_y, \omega) = \int_{-\infty}^{\infty} \int_{-\infty}^{\infty} \int_{-\infty}^{\infty} f(x, y, t) e^{-i(k_x x + k_y y - \omega t)} dx dy dt, \quad (34)$$

$$f(x, y, t) = \frac{1}{(2\pi)^3} \int_{-\infty}^{\infty} \int_{-\infty}^{\infty} \int_{-\infty}^{\infty} \hat{f}(k_x, k_y, \omega) e^{i(k_x x + k_y y - \omega t)} dk_x dk_y d\omega. \quad (35)$$

421 The translational invariance of the ocean response in the horizontal directions requires  
 422 that  $T$  depend on  $k_x$  and  $k_y$  only through the radial wavenumber  $k = (k_x^2 + k_y^2)^{1/2}$ .  
 423 Practically, 35 allows to analytically compute the sea surface response from seafloor up-  
 424 lift. Thereby, the (spectral) transfer function quantifies the ocean response to seafloor  
 425 uplift and contains within it information about wave modes in the ocean and how they  
 426 are excited by seafloor uplift.

The transfer function for the fully-coupled method (i.e., solution to the general prob-  
 lem, method 1) is (Lotto & Dunham, 2015; Wilson & Ma, 2021)

$$T_{gen}(k, \omega) = \frac{1}{\cosh(k^* H) - (gk^*/\omega^2) \sinh(k^* H)}, \quad (36)$$

where

$$k^* = \sqrt{k^2 - \omega^2/c_0^2}. \quad (37)$$

Poles in the transfer function correspond to the acoustic and surface gravity wave modes,  
 which have received extensive discussion in the literature (Levin et al., 2009). Briefly,

at a given wavenumber  $k$ , there are infinitely many solutions  $\omega$  to the dispersion relation. There is one surface gravity wave mode (indexed as  $n = 0$ ) and an infinite number of acoustic modes (indexed as  $n = 1, 2, \dots$ ). Fig. 3(a) shows the amplitude of the transfer function, with large amplitude response corresponding to  $(k, \omega)$  pairs satisfying the dispersion relation for surface gravity wave and acoustic modes. At small horizontal wavenumbers ( $kH \ll 1$ ), the surface gravity wave mode phase and group velocities asymptote to the nondispersive shallow water wave speed  $(gH)^{1/2}$ . The acoustic modes exist as propagating (rather than evanescent) modes only at frequencies greater than a cut-off frequency given approximately by

$$\omega_n \approx (n - 1/2)\pi c_0/H, \quad n = 1, 2, \dots, \quad (38)$$

427 and at large horizontal wavenumbers ( $kH \gg 1$ ), their phase and group velocities ap-  
 428 proach (from above and below, respectively) the sound speed  $c_0$ . We remark that replac-  
 429 ing the rigid seafloor condition with an elastic half-space (Section 6) modifies the wave  
 430 modes, especially the acoustic modes near their cut-off frequency (Eyov et al., 2013). Most  
 431 importantly, the  $n = 1$  mode no longer has a cut-off frequency, and transitions to an  
 432 oceanic Rayleigh wave (Biot, 1952) in the low frequency ( $\omega H/c_0 \ll 1$ ) limit. We ex-  
 433 plore this in more detail in Section 6.

In the incompressible limit,  $k^* \rightarrow k$  and the transfer function reduces to

$$T_{inc}(k, \omega) = \frac{1}{\cosh(kH) - (gk/\omega^2) \sinh(kH)}. \quad (39)$$

Surface gravity waves obey the dispersion relation  $\omega^2 = gk \tanh(kH)$ . Note also that the instantaneous ( $\omega \rightarrow \infty$ ) response is the well-known  $1/\cosh(kH)$  Kajiura filter (Kajiura, 1970). In the long wavelength ( $kH \ll 1$ ) limit, the incompressible transfer function is

$$T_{LLW}(k, \omega) = \frac{1}{1 - gHk^2/\omega^2}. \quad (40)$$

434 The absence of the  $1/\cosh(kH)$  filter means that all wavelengths of seafloor displace-  
 435 ments are transferred to the sea surface. Likewise, the surface gravity wave mode prop-  
 436 agates nondispersively at the shallow water speed:  $\omega/k = (gH)^{1/2}$  (Fig. 3d, bottom  
 437 panel). As the linear long wave model (used in methods 2,3) assumes an incompressible  
 438 ocean, its transfer function lacks acoustic wave modes (Fig. 3d, top panel).

The linear long wave model can be replaced with the Boussinesq model, which has transfer function

$$T_{Bous}(k, \omega) = \frac{1}{1 - \frac{gHk^2}{\omega^2} \left[ 1 + \frac{(kH)^2}{3} \right]}. \quad (41)$$

439 The associated dispersion relation,  $\omega^2 = gHk^2 \left[ 1 + (1/3)(kH)^2/3 \right]^{-1}$ , features a lead-  
 440 ing order dispersive correction to the linear long wave model.

The superposition method (method 4) sequentially solves two problems, using forcing from the first (zero-gravity) problem in the second (shallow water) problem. Its transfer function can therefore be factored as

$$T_{sup}(k, \omega) = T_{g=0}(k, \omega) T_{SW}(k, \omega), \quad (42)$$

in which

$$T_{g=0}(k, \omega) = \frac{1}{\cosh(k^*H)} \quad (43)$$

441 is obtained by setting  $g = 0$  in (36) and  $T_{SW}$  is given by either (40) or (41) for the lin-  
 442 ear long wave and Boussinesq models, respectively. The zero-gravity transfer function  
 443 (43) captures the acoustic modes of a compressible ocean bounded by a rigid bottom and

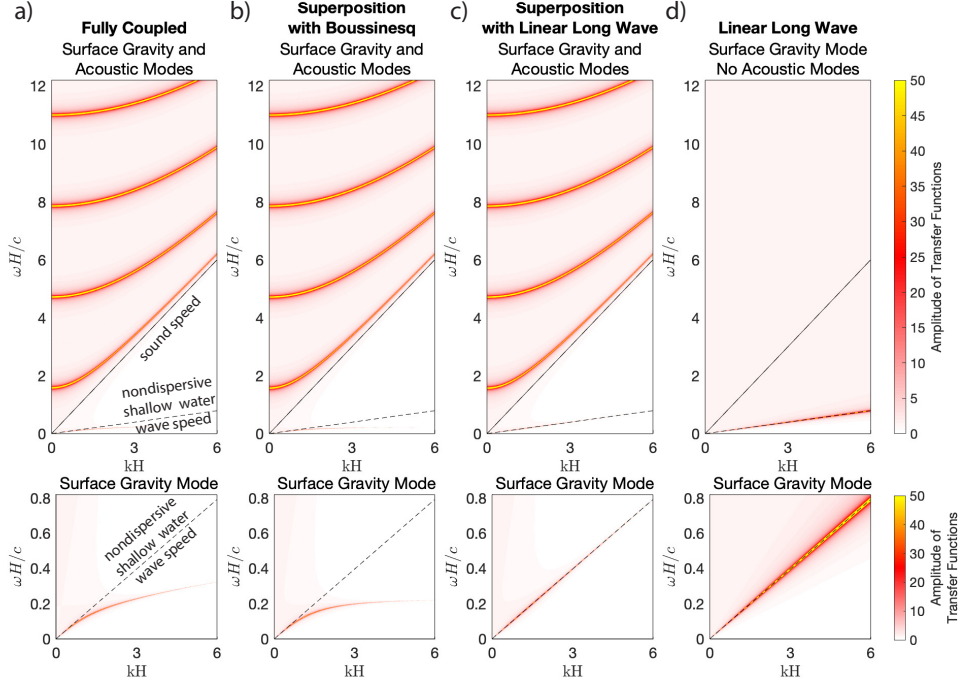


**Figure 3.** Amplitude of transfer functions for (a) fully coupled model, (b) superposition with Boussinesq model, (c) superposition with linear long wave model, (d) linear long wave model by itself. Top panels show higher values of  $\omega H/c$  to highlight acoustic modes, whereas bottom panels focus on the surface gravity wave mode.

444 free surface, so these modes are expressed in the transfer function for the superposition  
 445 method (Figs 3b and c, top panels). In addition, in the low frequency limit, or more pre-  
 446 cisely when horizontal phase velocity is much less than the sound speed ( $\omega/(kc_0) \ll 1$ ),  
 447 then  $k^* \rightarrow k$  and the transfer function reduces to the  $1/\cosh(kH)$  filter (Kajiura, 1970).  
 448 Thus, the superposition method captures nonhydrostatic ocean response at short wave-  
 449 lengths during the tsunami generation process, even when a linear long wave model is  
 450 used for tsunami propagation. This is evident in the decreasing amplitude of the trans-  
 451 fer function for large  $kH$  (Figs 3b and c, bottom panels) in contrast to what is seen for  
 452 the linear long wave model as used in methods 2 and 3 (Fig. 3d, bottom panel). On the  
 453 other hand, dispersion is neglected during tsunami propagation when using a nondisper-  
 454 sive linear long wave solver, but is captured (approximately) by using a weakly disper-  
 455 sive Boussinesq solver (compare Figs 3b and c, bottom panels).

## 456 5 Comparing the four modeling methods using an imposed Gaussian 457 seafloor displacement

In this section, we perform 3D numerical simulations to study the wave response of a uniform depth ocean to an imposed seafloor displacement. There is no coupling to an elastic solid. The seafloor uplift rate is a Gaussian in both space and time,

$$\partial b/\partial t = \left( A/(\sigma_t \sqrt{2\pi}) \right) \exp \left( -(t - 4\sigma_t)^2 / 2\sigma_t^2 \right) \exp \left( -(x^2 + y^2) / 2\sigma_r^2 \right), \quad (44)$$

458 where  $\sigma_r$  and  $\sigma_t$  characterize the spatial width and duration of the source. The maxi-  
 459 mum uplift rate occurs at time  $t = 4\sigma_t$  so that the simulation can begin with effectively  
 460 zero uplift rate at  $t = 0$ . We fix  $H = 4$  km,  $c_0 = 1.5$  km/s, and  $g = 9.81$  m/s<sup>2</sup>, and  
 461 vary  $\sigma_r$  and  $\sigma_t$  across three scenarios. We set up scenarios to allow for different excita-  
 462 tion of tsunami and acoustic waves, showing results for a long duration source, an im-  
 463 pulsive source, and an impulsive source with a narrow source width to produce short wave-  
 464 lengths for which we anticipate dispersion and filtering effects in the ocean response (Ta-  
 465 ble 1).

466 For the three scenarios, domain sizes, discretization, and simulation time varied to  
 467 best capture important features in the wavefield. The horizontal domain size was large  
 468 enough to avoid boundary reflections. The element size was set to a uniform character-  
 469 istic edge length in the interior region of the domain and increased to a larger charac-  
 470 teristic length outside this region. For scenario 1, the domain was 500 km by 500 km with  
 471 an interior region 300 km by 300 km with a characteristic element edge length of 1.5 km  
 472 and an outer characteristic element length of 75 km; the simulation was run for 800 s.  
 473 For scenario 2, the domain was 200 km by 200 km with an interior region 110 km by 110  
 474 km with a characteristic element length of 1 km and an outer characteristic element length  
 475 of 75 km; the simulation was run for 400 s. For scenario 3, the domain was 400 km by  
 476 400 km with an interior region 40 km by 40 km with a characteristic element edge length  
 477 of 0.25 km and an outer characteristic element edge length of 25 km; the simulation was  
 478 run for 150 s.

**Table 1.** Three scenarios involving a prescribed seafloor uplift rate that is Gaussian in space and time, with width  $\sigma_r$  and duration  $\sigma_t$ . Three non-dimensional parameters control the solution and validity of the assumptions used in modeling methods 2-4.

	Source width $\sigma_r$ (km)	Source duration $\sigma_t$ (s)	Instantaneous source $\sqrt{gH}\sigma_t/\sigma_r \ll 1$	Negligible acoustic wave excitation $H/(c_0\sigma_t) \ll 1$	Shallow water limit $H/\sigma_r \ll 1$
Scenario 1	12.5	125	Violated	Justified	Justified
Scenario 2	12.5	1.25	Justified	Violated	Justified
Scenario 3	1.25	1.25	Justified	Violated	Violated

### 479 5.1 Ocean transfer function and source spectrum determine excitation 480 of wave modes

The transfer functions derived previously allow us to anticipate the wave modes that will be excited by the imposed seafloor displacement. Fourier transforming  $b(x, y, t)$  using (34) gives

$$\hat{b}(k, \omega) = \frac{A}{-i\omega} 2\pi\sigma_r^2 \exp(-\sigma_t^2\omega^2/2 + 4i\sigma_t\omega) \exp(-\sigma_r^2k^2/2). \quad (45)$$

481 This source primarily excites waves having angular frequencies below  $\sigma_t^{-1}$  and wavenum-  
 482 bers below  $\sigma_r^{-1}$ . Given the seafloor displacement spectrum  $\hat{b}(k, \omega)$ , the sea surface spec-  
 483 tral response can be calculated using the transfer function as  $\hat{\eta}(k, \omega) = T(k, \omega)\hat{b}(k, \omega)$ .  
 484 Fig. 4 shows the imposed seafloor displacement spectrum and the sea surface response  
 485 for the four modeling methods.

486 Scenario 1 (Fig. 4, left column) is a long duration source ( $\sigma_t = 125$  s). Because  
 487  $H/(c_0\sigma_t) \ll 1$ , the excitation occurs only for angular frequencies satisfying  $\omega H/c_0 \ll$   
 488 1. Compressibility effects in the ocean are negligible, so only surface gravity waves are



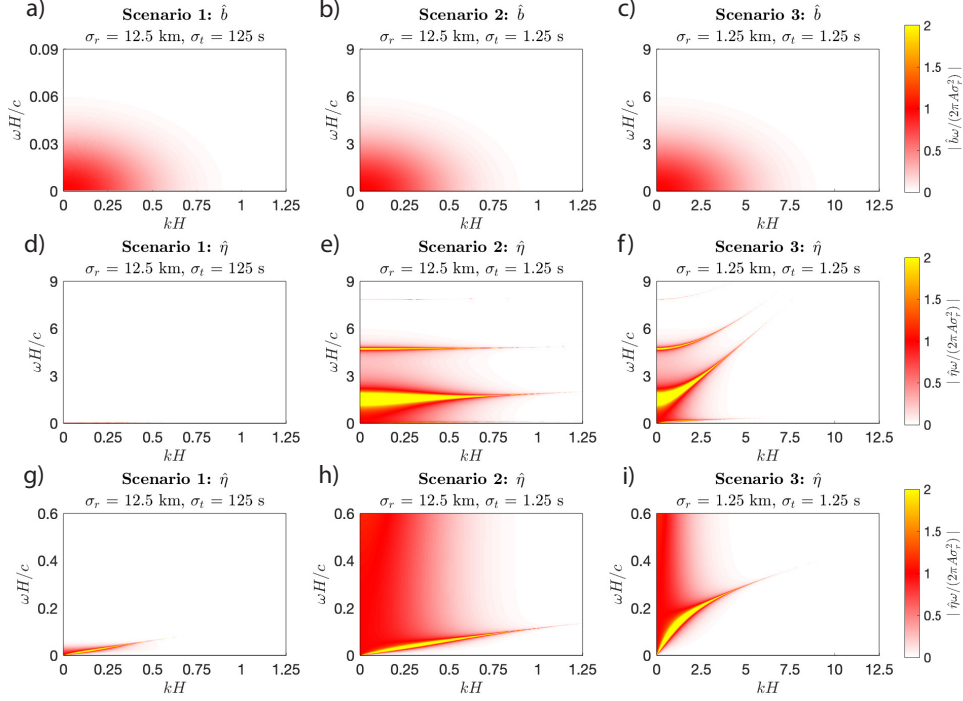


**Figure 4.** Fourier domain seafloor displacement (a-c) and sea surface response (d-i) for three scenarios having different spatial widths  $\sigma_r$  and durations  $\sigma_t$  of the imposed seafloor displacement. The long duration of scenario 1 prevents excitation of acoustic wave modes, in contrast to the shorter duration scenarios 2 and 3. The long duration also requires accounting for tsunami propagation during the wave generation process. The narrower width of scenario 3 produces dispersion of the surface gravity wave mode.

489 generated, in contrast to the shorter duration sources ( $\sigma_t = 1.25$  s) in scenarios 2 and  
 490 3 (Fig. 4, middle and right columns) that also excite acoustic waves.

491 Scenarios 2 and 3 differ in the source width  $\sigma_r$ , with the narrow width in scenario  
 492 3 leading to pronounced dispersion of the surface gravity wave mode and the filtering  
 493 of short wavelengths when translating seafloor displacement to sea surface displacement.  
 494 The relevant dimensionless parameter determining this behavior is  $H/\sigma_r$ .

495 Finally, scenario 1 provides an example of a long duration source for which tsunami  
 496 propagation occurs during the wave generation process, violating one of the assumptions  
 497 made for method 2. The importance of this effect can be assessed by comparing the tsunami  
 498 propagation distance during the earthquake duration,  $\sqrt{gH}\sigma_t$ , to the spatial extent of  
 499 the source,  $\sigma_r$ . When  $\sqrt{gH}\sigma_t/\sigma_r \ll 1$ , then the source is effectively instantaneous; oth-  
 500 erwise a time-dependent tsunami source must be considered.

501 To summarize, we have identified three dimensionless parameters that control the  
 502 solution behavior for our Gaussian source, specifically the excitation of acoustic waves  
 503 ( $H/(c_0\sigma_t)$ ), shallow water limit ( $H/\sigma_r$ ), and whether tsunami propagation will occur over  
 504 the source duration ( $\sqrt{gH}\sigma_t/\sigma_r$ ). These dimensionless parameters can be used to de-  
 505 termine if the assumptions of modeling methods 2-4 are justified and to anticipate what  
 506 solution features will be inaccurate when these assumptions are violated.

## 5.2 Numerical simulations of the ocean response to an imposed Gaussian seafloor displacement

Next we apply the four modeling methods to this problem, using numerical simulations that are implemented as described in Section 3.5. Results are shown in Fig. 5. For this problem, the shallow water solver used in methods 2-4 is the nondispersive linear long wave model, and we do not apply the Kajiura filter for methods 2 and 3. For the instantaneous source model 2, we set the initial sea surface height to be equal to the seafloor displacement at the end of the earthquake simulation; at this point the seafloor is no longer deforming. We shift the start time of the tsunami to the time at which the Gaussian uplift rate is maximum.

Scenario 1 (Fig. 5, top row) features a wide, long duration source. The ocean responds in the shallow water limit, with negligible filtering of short wavelengths during tsunami generation and dispersion during tsunami propagation. The long duration implies that acoustic wave excitation is negligible and that the tsunami propagates over the source duration. The main feature in all four methods is the tsunami wave propagating with velocity  $(gH)^{1/2}$ . Methods 1, 3, and 4, which all account for the finite duration of the source, produce visually identical solutions. The instantaneous source method 2 differs from the other modeling methods; it overpredicts the tsunami amplitude and underpredicts the tsunami period.

Scenario 2 (Fig. 5, middle row) has the same wide source width as scenario 1 and all four methods accurately capture the tsunami, which propagates with negligible dispersion. The source duration is much shorter, explaining why here the instantaneous source method 2 matches the time-dependent source method 3. The shorter duration source excites acoustic waves, which produce a beating pattern in the space-time plots. The long horizontal wavelength of these waves causes them to be almost vertically propagating, with a horizontal phase velocity that exceeds the sound speed. Methods 1 and 4, which capture acoustic waves, show excellent agreement.

Scenario 3 has the same short duration source as scenario 2, such that acoustic waves are excited, but with a narrower source width. The narrow width excites short wavelength surface gravity waves that violate the shallow water condition  $kH \ll 1$ , leading to dispersion during propagation. This dispersion is captured only in method 1, but not any of the other methods because we use a linear long wave model. The other relevant non-hydrostatic effect is the filtering of short wavelengths in the transfer function between seafloor uplift and sea surface response (Kajiura, 1963). This filtering reduces tsunami wave amplitude by over a factor of two in this example and also changes the waveform shape. Method 4 accounts for this filtering effect through the initial zero-gravity simulation that includes a depth-resolved ocean response, even when a nondispersive linear long wave model is used for tsunami propagation. Thus the tsunami predicted by method 4 agrees much better with that of method 1 than methods 2 and 3, which neglect the filtering effect. The differences between methods 1 and 4 appear only during tsunami propagation, manifesting mainly as dispersion-related features in the trailing edge of the tsunami wave.

Returning to the acoustic waves, we examine which acoustic modes are contributing to the response in scenarios 2 and 3. The transfer function analysis (Fig. 4) shows that the first two acoustic modes should be excited. However, the amplitude of the first acoustic mode is much larger and is expressed over a wider range of frequencies than the second acoustic mode. To confirm this, we perform a spectral analysis (using a discrete Fourier transform in space and time) of the sea surface displacement field from the method 1 numerical solution for scenario 3 and compare this to the analytical solution derived earlier. Results, shown in Fig. 6, show excellent agreement between the numerical and analytical solutions. Thus we conclude that the acoustic wavefield is dominated by the first acoustic mode.

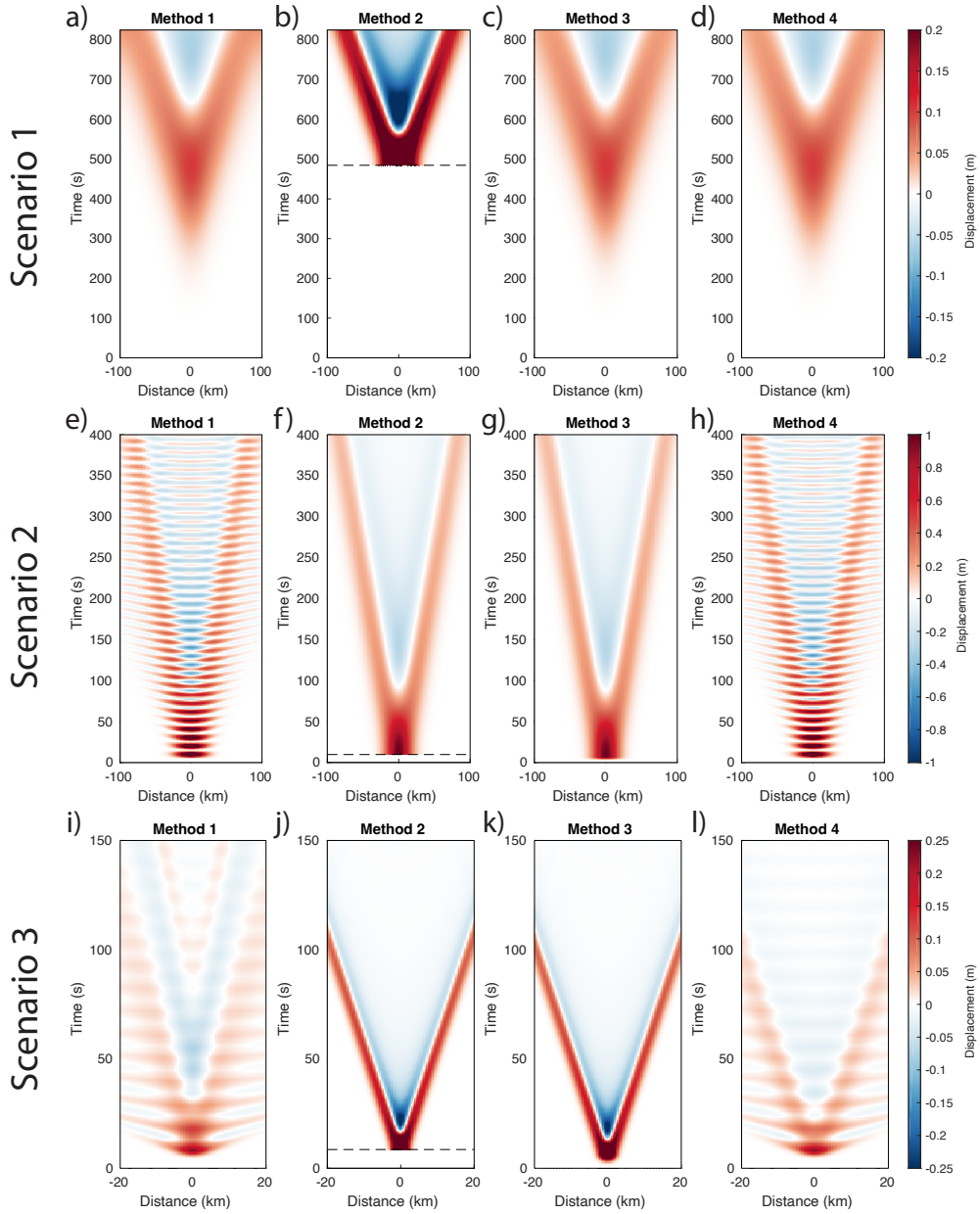


**Figure 5.** Simulation results of sea surface displacement, plotting along an arbitrary cross-section through the center of the source, for the three scenarios (panel rows) using the four modeling methods (panel columns). Scenario 1: For this long duration source, tsunami propagation during the wave excitation process leads to reduced amplitudes as compared to the method 2 assumption of an instantaneous source. Negligible acoustic waves are excited. Scenario 2: The shorter source duration excites acoustic waves. Scenario 3: The narrower source violates the shallow water limit, leading to filtering of short wavelength and dispersion of surface gravity waves.

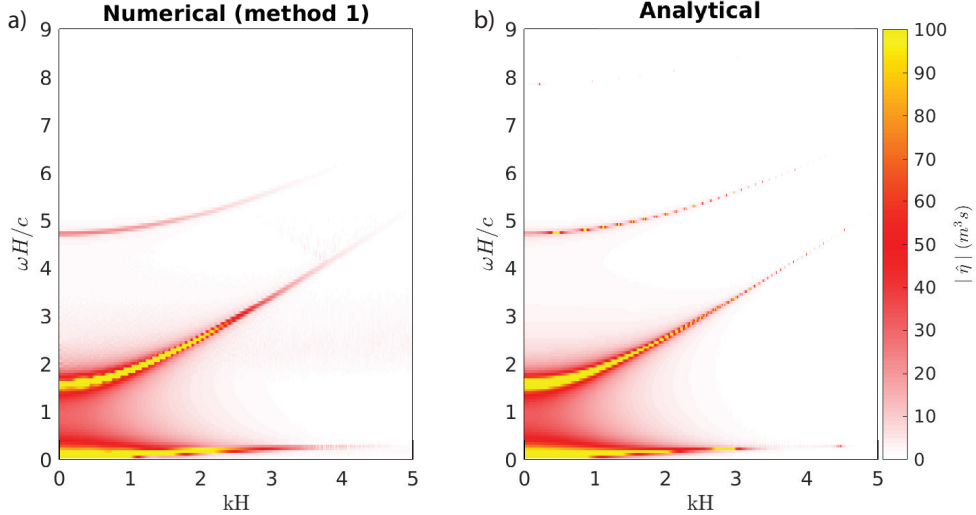


**Figure 6.** Fourier spectral amplitude of sea surface displacement for scenario 3: (a) method 1 (fully-coupled method), computed using FFTs in space and time, (b) analytical solution obtained using the transfer function. The color scale for spectral amplitude is less saturated than in Fig. 4 in order to more clearly emphasize the very weak excitation of the second acoustic mode as compared to the first acoustic mode.

## 6 Effects of an elastic seafloor on wave modes

Thus far, we have focused our analysis of wave excitation on an ocean with a seafloor that is rigid, except when prescribing seafloor uplift. Here we extend this analysis by accounting for an elastic half-space underlying the ocean. Our implementation of the fully coupled method in SeisSol permits the simulation of kinematic or dynamic rupture sources with self-consistent excitation of waves in the solid and overlying ocean. While the elasticity of the seafloor has a negligible effect on tsunami generation and propagation, at least for the local and regional scale problems considered in this study, there are pronounced changes to the acoustic response. Specifically, elasticity removes the cut-off frequency of the first acoustic mode, and that mode transitions into a Rayleigh wave as  $\omega H/c_0 \rightarrow 0$ . Hence, there is no clear distinction between seismic and acoustic wave modes in this problem. We examine dispersion properties of this so-called oceanic Rayleigh wave (Biot, 1952) and illustrate how the interplay between the frequencies of the source and the frequency at which group velocity has a local minimum determines the expression of this wave mode, specifically the generation of an Airy phase.

An appropriate starting point for our discussion is the dispersion relation for a homogeneous acoustic layer (ocean) of thickness  $H$ , density  $\rho$ , and sound speed  $c_0$  over a homogeneous elastic half-space of density  $\rho_s$  and P- and S-wave speeds  $c_p$  and  $c_s$ . We neglect gravity in this analysis and utilize a standard  $p = 0$  free surface condition on the ocean surface. Given an angular frequency  $\omega$ , we solve the dispersion relation for horizontal wavenumbers  $k$ . For a sufficiently high frequency there are multiple solutions, indexed by the integer  $n$  (and starting at  $n = 1$  rather than with the  $n = 0$  surface gravity wave mode because gravity is neglected). Here we focus exclusively on the  $n = 1$  oceanic Rayleigh wave mode.

Defining horizontal phase velocity  $c = \omega/k$ , the dispersion relation is (Biot, 1952; Eyov et al., 2013)

$$4\alpha_s\alpha_p - (1 + \alpha_s^2)^2 = \frac{\rho c^4}{\rho_s c_s^4} \frac{\alpha_p}{\alpha_0} \tan\left(\frac{\alpha_0 \omega H}{c}\right), \quad (46)$$

where

$$\alpha_p = \sqrt{1 - \frac{c^2}{c_p^2}}, \quad \alpha_s = \sqrt{1 - \frac{c^2}{c_s^2}}, \quad \text{and} \quad \alpha_0 = \sqrt{\frac{c^2}{c_0^2} - 1}. \quad (47)$$

The left-hand side of (46) is the Rayleigh function

$$R(c) = 4\alpha_s\alpha_p - (1 + \alpha_s^2)^2, \quad (48)$$

583 which has a single nondispersive solution  $c_R$  that satisfies  $R(c_R) = 0$ . When  $\omega H/c_0 \rightarrow$   
 584 0, the right side of (46) also goes to zero. In this limit, the ocean response becomes neg-  
 585 ligible and the solution approaches the nondispersive Rayleigh wave in the elastic half-  
 586 space. In the opposite limit  $\omega H/c_0 \rightarrow \infty$ , the solution becomes a nondispersive Scholte  
 587 wave propagating at the elastic-acoustic interface and having velocity only slightly less  
 588 than  $c_0$  (Biot, 1952). Of particular note is that this  $n = 1$  mode exists for all frequen-  
 589 cies, in contrast to the case of a compressible ocean with a rigid bottom. Like the rigid-  
 590 bottom case, the elastic-bottom case has higher mode solutions that exist only above a  
 591 cut-off frequency (Biot, 1952; Eyov et al., 2013). These higher modes are appreciably  
 592 excited in our simulations due to the smoothness of the source.

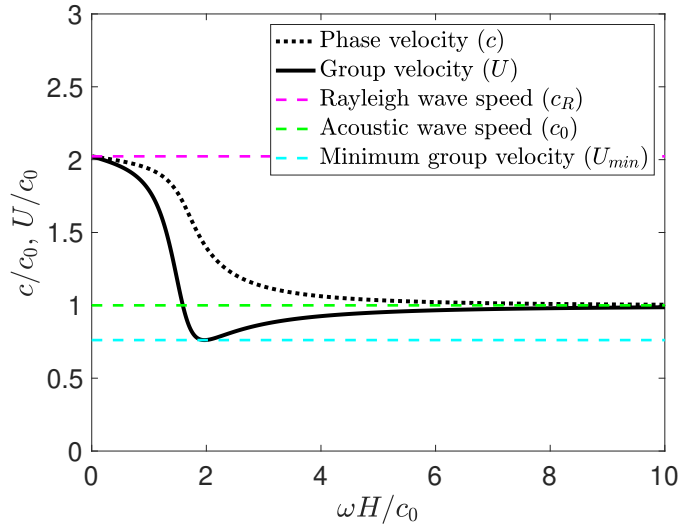


**Figure 7.** Phase ( $c$ ) and group velocity ( $U$ ), normalized by the ocean sound speed  $c_0$ , for the  $n = 1$  oceanic Rayleigh wave mode as a function of dimensionless angular frequency ( $\omega H/c_0$ ). Also shown as horizontal lines are the Rayleigh wave speed of the solid ( $c_R$ ), to which both  $c$  and  $U$  approach as  $\omega H/c_0 \rightarrow 0$ ; the ocean acoustic wave speed ( $c_0$ ); and the minimum group velocity ( $U_{\min}$ ).

593 Fig. 6 shows the phase velocity ( $c = \omega/k$ ) and group velocity ( $U = d\omega/dk$ ) for  
 594 the  $n = 1$  oceanic Rayleigh wave mode. The group velocity reaches a minimum,  $U_{\min}$ ,  
 595 at a frequency  $f_{\min}$  that is slightly greater than the cut-off frequency of the  $n = 1$  mode  
 596 for a rigid-bottom ocean ( $f = c_0/(4H)$  or  $\omega H/c_0 = \pi/2$ ), reflecting a resonance con-  
 597 dition within the ocean. The minimum group velocity is less than the ocean sound speed  
 598 ( $U_{\min} < c_0$ ). Normal dispersion ( $dU/d\omega < 0$ ) occurs for frequencies lower than the

599 minimum in group velocity. Anomalous dispersion ( $dU/d\omega > 0$ ) occurs at higher fre-  
 600 quencies.

601 The structure of the dispersion curve controls the expression of oceanic Rayleigh  
 602 waves from an earthquake source, as we demonstrate with numerical simulations in the  
 603 following section. However, following Aki and Richards (2002, Ch. 7.1), we can antic-  
 604 ipate key features of the wavefield. Consider the response at fixed horizontal distance  
 605  $r$  away from the source. The initial oceanic Rayleigh wave arrivals, appearing at time  
 606  $t = r/c_R$ , have the lowest frequencies. The dominant frequency then increases with time  
 607 as normally dispersed waves with slower group velocities arrive. This continues until ap-  
 608 proximately  $t = r/c_0$ , at which time there exist two solutions to the dispersion rela-  
 609 tion having identical group velocities. One solution (with normal dispersion) continues  
 610 the increasing frequency trend seen earlier, while the second (with anomalous dispersion)  
 611 appears at a much higher frequency that decreases with time. This superposition of nor-  
 612 mally and anomalously dispersed waves continues until the arrival of the Airy phase at  
 613  $t = r/U_{\min}$ . The relative amplitude of the normally and anomalously dispersed waves  
 614 depends, in part, on the source spectrum. In particular, the wavefield of a source that  
 615 excites no waves above the frequency of minimum group velocity  $f_{\min}$  will lack the anoma-  
 616 lously dispersed waves and Airy phase. This condition can be met by a low frequency  
 617 source spectrum or by having a sufficiently shallow ocean.

## 618 7 Dynamic rupture simulations and oceanic Rayleigh waves

619 In this section we complement our previous numerical simulations of the ocean re-  
 620 sponse to an imposed Gaussian-shaped seafloor uplift with dynamic rupture simulations  
 621 in a coupled ocean-solid Earth material structure (Fig. 8). Specifically, we compare the  
 622 four modeling methods with a dynamic rupture source and varying water depth to show  
 623 the effect of water depth on the excitation and propagation of the tsunami, acoustic, and  
 624 seismic waves. We use only the linear long wave model for tsunami propagation in meth-  
 625 ods 2 and 3, but we use both linear long wave and Boussinesq models for method 4 to  
 626 illustrate the importance of accounting for dispersive tsunami propagation.

### 627 7.1 Problem setup

The dynamic rupture simulation is conducted for a low angle thrust fault in a ho-  
 mogeneous elastic half-space overlain by a compressible ocean of uniform depth  $H$ . The  
 $x$  axis follows the strike of the fault with  $y$  being the other horizontal direction perpen-  
 dicular to strike (with the fault dipping in the  $-y$  direction) and  $z$  being vertical (pos-  
 itive up with  $z = 0$  at the seafloor). Parameter values are given in Table 2. The pla-  
 nar rectangular fault having along-strike length of 30 km dips  $15^\circ$  with respect to the  
 seafloor. Initial stress conditions assume pore fluid overpressure with effective principal  
 stresses increasing linearly with depth as

$$\sigma'_{yy}(z) = (C - \lambda)\rho_s gz, \quad \sigma'_{zz}(z) = (1 - \lambda)\rho_s gz, \quad (49)$$

628 and  $\sigma'_{xx} = (\sigma'_{yy} + \sigma'_{zz})/2$ . We choose the constant principal stress ratio  $C = 1.5$  and  
 629 the Hubbert-Rubey pore fluid pressure ratio  $\lambda = \rho/\rho_s + 0.4574$  to produce a reason-  
 630 able stress drop after selecting friction parameters. Below a down-dip distance of 13.8  
 631 km, all principal stresses are set to lithostatic to arrest the rupture and limit the down-  
 632 dip extent of slip. The simulations are set up to allow for overpressured portion of the  
 633 fault to slip once nucleated, here we specifically set up simulations to have the fault to  
 634 slip to the surface.

635 We use linear slip-weakening friction with cohesion. The rupture is initiated by re-  
 636 ducing the static friction coefficient in a square nucleation zone having length and width

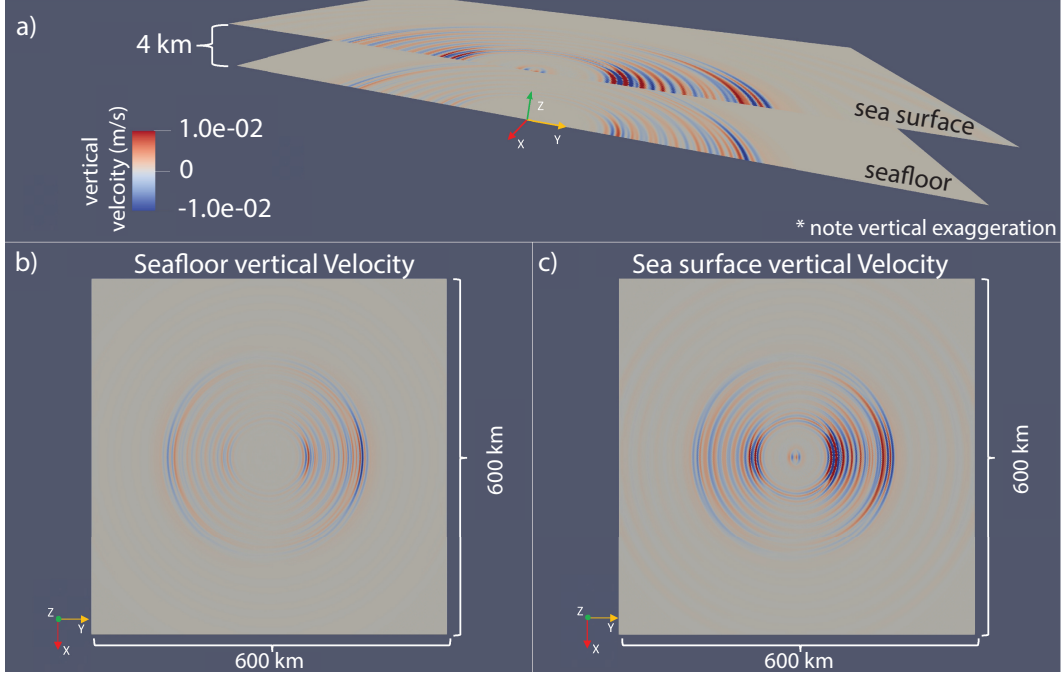


**Figure 8.** Dynamic rupture on a shallow thrust fault causes the seafloor to deform and the ocean to respond. Shown is the vertical velocity for a fully-coupled method simulation for an ocean of depth  $H = 4$  km at  $t = 120$  s. (a) Half the domain is shown (sliced across strike for ease of visualizing both surfaces), with the seafloor below and sea surface above. (b) Vertical velocity on the seafloor. (c) Vertical velocity on sea surface.

637 of 3 km, centered 12 km down-dip, so that the prescribed initial stress exceeds peak strength  
 638 in this region at the start of the simulation (Harris et al., 2011, 2018).

639 The computational domain has an acoustic ocean (of depth  $H = 4$  km) above a  
 640 220 km deep elastic Earth, stretching 1200 km in both horizontal directions, with ab-  
 641 sorbing boundary conditions on the sides and bottom boundaries. We use an unstruc-  
 642 tured tetrahedral mesh. The element size increases from 100 m around the fault nucle-  
 643 ation zone to 250 m on the edges of the fault. Away from the fault, the element size in-  
 644 creases gradually to 7.5 km.

645 For modeling methods requiring a separate tsunami simulation, the solution is in-  
 646 terpolated onto a Cartesian mesh. This is then used as input for the tsunami model. For  
 647 the linear long wave tsunami solver (FDMAP), we divided the 600 km by 600 km do-  
 648 main into an interior region of 400 km by 400 km with 1 km grid spacing and outer re-  
 649 gion in which grid spacing increases to 10 km. For the Boussinesq tsunami solver, the  
 650 400 km by 400 km domain has a uniform 1 km grid spacing.

## 651 7.2 Comparison of modeling methods

652 Fig. 9 shows the rupture history and seafloor and sea surface displacements from  
 653 a simulation with no gravity and  $H = 4$  km. Rupture propagates up-dip, exciting oceanic  
 654 Rayleigh waves and leaving a static displacement of both the seafloor and sea surface.  
 655 Method 2 uses the final static seafloor displacement at 350 s (Fig. 9b) as the tsunami  
 656 initial condition. Method 3 uses forcing from the seafloor velocity (Fig. 9c). Method 4  
 657 uses forcing from the sea surface velocity (Fig. 9d). The rupture process and seafloor

**Table 2.** Parameter values for dynamic rupture simulations.

parameter	symbol	value
Density in ocean	$\rho$	1000 kg/m <sup>3</sup>
Sound speed in ocean	$c_0$	1500 m/s
Density in solid	$\rho_s$	2700 kg/m <sup>3</sup>
Gravity	$g$	9.81 m/s <sup>2</sup>
P-wave speed in solid	$c_p$	5716 m/s
S-wave speed in solid	$c_s$	3300 m/s
Ocean depth	$H$	variable
Fault dip	$\theta$	15°
Fault length along-strike		30 km
Fault length down-dip		15 km
Static friction inside nucleation zone	$\mu_{s,in}$	0.57
Static friction outside nucleation zone	$\mu_{s,out}$	0.60
Dynamic friction	$\mu_d$	0.40
Slip-weakening distance	$D_c$	0.3 m
Cohesion	$c$	0.15 MPa
Principal stress ratio parameter	$C$	1.5
Hubbert-Rubey pore fluid pressure ratio	$\lambda$	0.82777

658 displacements are similar, though not identical, for other ocean depths, confirming the  
659 relatively small feedback from the ocean onto the fault that was noted by Kozdon and  
660 Dunham (2013).

661 Fig. 10 shows the vertical sea surface velocity for the four modeling methods for  
662  $H = 4$  km. Examining tsunami generation and propagation in the four methods, we  
663 see differences in amplitude and waveform shape. Methods 2 and 3 (Figs 10b, c, f) over-  
664 predict the tsunami wave amplitude by a factor of two because the non-hydrostatic fil-  
665 tering effect of the ocean is neglected in the tsunami generation process when translat-  
666 ing between the seafloor and sea surface. This discrepancy can be reduced using a Ka-  
667 jiuira filter, which we have not applied in these examples. Method 4 captures the filter-  
668 ing effect during tsunami generation, so tsunami amplitudes are more consistent with  
669 method 1. Whereas we use only the nondispersive linear long wave model for tsunami  
670 propagation in methods 2 and 3, we compare two versions of method 4, one that uses  
671 the linear long wave model (Fig. 10d) and a second that uses the weakly dispersive Boussi-  
672 nesq model (Fig. 10d). While the initial tsunami is similar in these two versions of method  
673 4, the tsunami waveform becomes increasingly dissimilar as time progresses (Fig. 10f).  
674 The Boussinesq model shows the best agreement with method 1, while the linear long  
675 wave model incorrectly predicts a much larger initial wave that arrives too early.

676 Fig. 10(g) compares seismic and acoustic wave propagation. Seismic and acous-  
677 tic waves are absent for method 2, which uses the final seafloor displacement as an ini-  
678 tial condition for the tsunami simulation. Methods 1, 3, and 4 all feature seismic and  
679 acoustic waves, with the largest amplitude waves being oceanic Rayleigh waves that show  
680 enhanced amplitudes in the  $+y$  direction of up-dip rupture propagation (Figs 10a, c, d,  
681 e). Both methods 3 and 4 use time-dependent forcing that includes seismic/acoustic waves  
682 from the zero gravity simulation, but method 3 uses forcing from the seafloor and method  
683 4 from the sea surface. This causes method 3 to have an incorrect amplitude for the seis-  
684 mic/acoustic waves (Fig. 10c). This is also evident in a seismogram for a single receiver  
685 on the sea surface at  $x = 0$ ,  $y = 100$  km (Fig. 10g). We note that some implementa-  
686 tions of method 3 filter the seafloor displacement to eliminate these acoustic/seismic waves



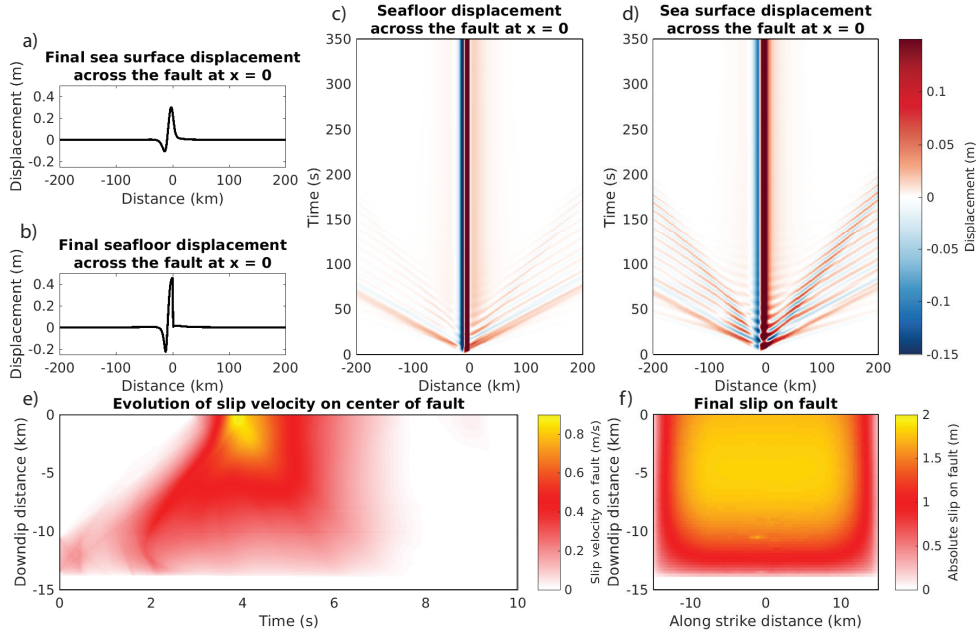


**Figure 9.** Dynamic rupture simulation with ocean depth  $H = 4$  km and no gravity. Space-time plots of (c) seafloor and (d) sea surface vertical displacement along a cross-section perpendicular to strike through the center of the fault, with static displacements (at  $t = 350$  s) shown in (a) and (b). (e) Space-time plot of slip velocity along a cross-section extending down-dip through the center of the fault. (f) Final slip on fault.

687 (Madden et al., 2021; Aniko Wirp et al., 2021) to focus exclusively on the tsunami. In  
 688 contrast, method 4 produces nearly identical seismic/acoustic waves to method 1. Slight  
 689 differences may be caused by the lack of restoring force from gravity on the acoustic waves.  
 690 Negligible differences are seen between the linear long wave and Boussinesq versions of  
 691 method 4.

692 We repeated this scenario for shallower depth oceans ( $H = 0.4$  km and  $H = 1$   
 693 km). Results for  $H = 1$  km are shown in Figs. 11 and 12. While the rupture histories  
 694 are similar to the  $H = 4$  km case, seismic and acoustic waves become less pronounced  
 695 as  $H$  is decreased. In the next section we explain how  $H$  influences the seismic/acoustic  
 696 wavefield.

### 697 7.3 Source spectrum and ocean depth control expression of oceanic Rayleigh 698 waves

699 Our simulations feature prominent oceanic Rayleigh waves, which are the gener-  
 700 alization of acoustic waves modes in a rigid-bottomed ocean when accounting for the elas-  
 701 ticity of the solid. Ocean depth  $H$  alters the dispersion properties of oceanic Rayleigh  
 702 waves, in particular the frequency  $f_{\min}$  at which the group velocity has a minimum  $U_{\min}$ .  
 703 The dynamic rupture excites frequencies below some maximum frequency, which we find  
 704 is approximately independent of ocean depth (because the ocean has only a small influ-  
 705 ence on the dynamic rupture process). We explain how the character of the oceanic Rayleigh  
 706 waves changes with ocean depth.

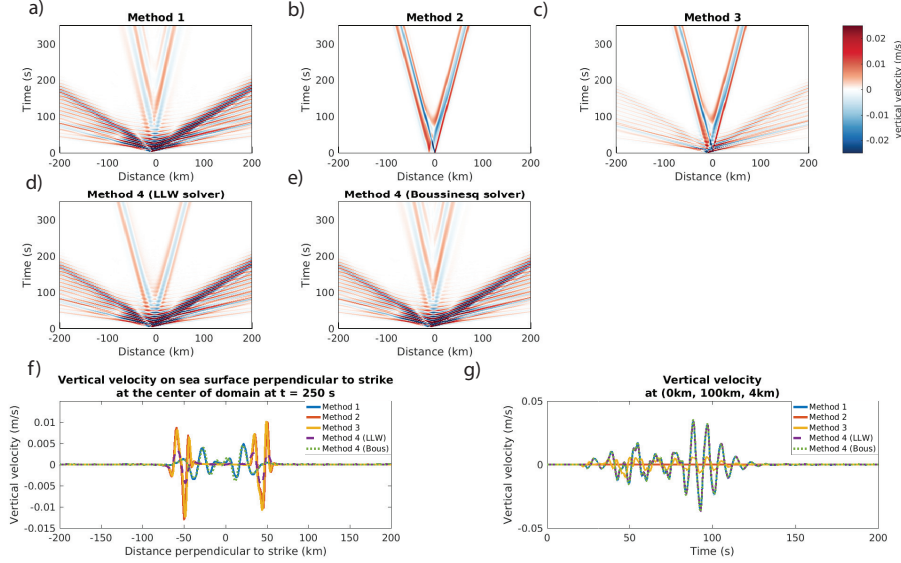


**Figure 10.** (a-e) Sea surface vertical velocity along a cross-section perpendicular to strike through the center of the fault for the four modeling methods with an ocean depth of  $H = 4$  km. a) Method 1 (fully-coupled method), b) Method 2 (instantaneous source method), c) Method 3 (time-dependent source method), d) Method 4 with a linear long wave (LLW) solver (superposition method), e) Method 4 with a Boussinesq (Bous) solver (superposition method). While both variants of method 4 account for nonhydrostatic filtering effects during tsunami generation, only the Boussinesq model accurately captures dispersion during tsunami propagation. f) Tsunami wave highlighted at single time  $t = 250$  s, on the sea surface perpendicular to strike at the center of the domain, and g) Seismic/acoustic wave highlighted at a single receiver located on the sea surface at  $x = 0$ ,  $y = 100$  km.

707 Fig. 13 shows space-time plots of sea surface vertical velocity from the fully-coupled  
 708 method 1 for ocean depths of  $H = 0.4$  km, 1 km, and 4 km, along with lines showing  
 709 the Rayleigh wave speed of the solid  $c_R$ , ocean sound speed  $c_0$ , and minimum group ve-  
 710 locity  $U_{\min}$  (see also the dispersion curve in Fig. 6, which is repeated in Fig. 13d). Also  
 711 shown are moment rate spectra of the ruptures, which help to quantify the frequency  
 712 content of waves excited by the source. However, for a finite source the radiated wave  
 713 spectra vary with direction due to directivity effects, so we also plot spectra of sea sur-  
 714 face velocity at a point in the forward direction. The initial arrivals in the space-time  
 715 plots are PL waves (Kozdon & Dunham, 2014; Wilson & Ma, 2021), which are followed  
 716 by a larger amplitude, dispersed wave packet of oceanic Rayleigh waves.

717 The leading edge of this wave packet propagates at speed  $c_R$ , and arrives imme-  
 718 diately after it exhibits normal dispersion. These correspond to the normally dispersed  
 719 branch of the dispersion curve at frequencies less than  $f_{\min}$ . Amplitudes are largest at  
 720 the leading edge of this wave packet for the shallow water ( $H = 0.4$  km and  $H = 1$   
 721 km) cases. In contrast, the deep water ( $H = 4$  km) case has an additional, larger am-  
 722 plitude set of waves whose leading edge propagates a bit slower than  $c_0$ . These corre-  
 723 spond to the anomalously dispersed branch on the dispersion curve at frequencies greater  
 724 than  $f_{\min}$ . The wave packet terminates with the Airy phase. The anomalously dispersed  
 725 waves and Airy phase are not seen in the  $H = 0.4$  km and  $H = 1$  km cases because  
 726  $f_{\min}$  is larger than the maximum source frequency. Thus we conclude that the source

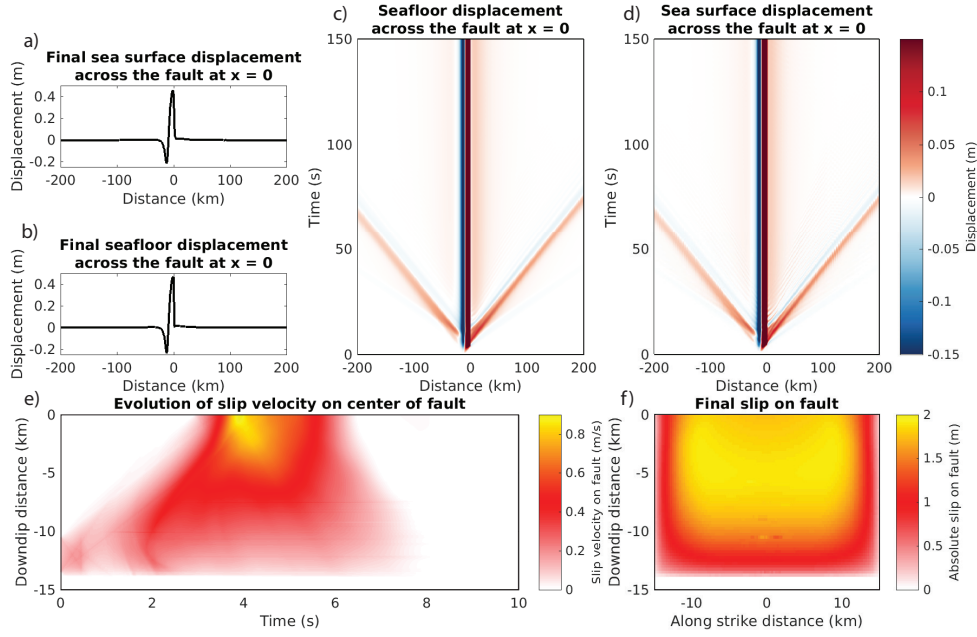


Figure 11. Same as Fig. 9 except for  $H = 1$  km.

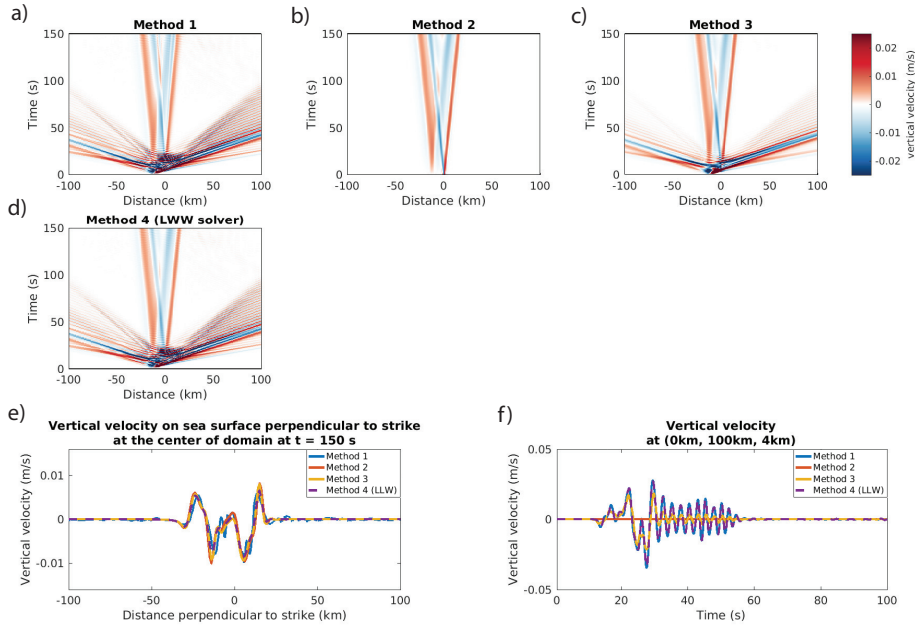
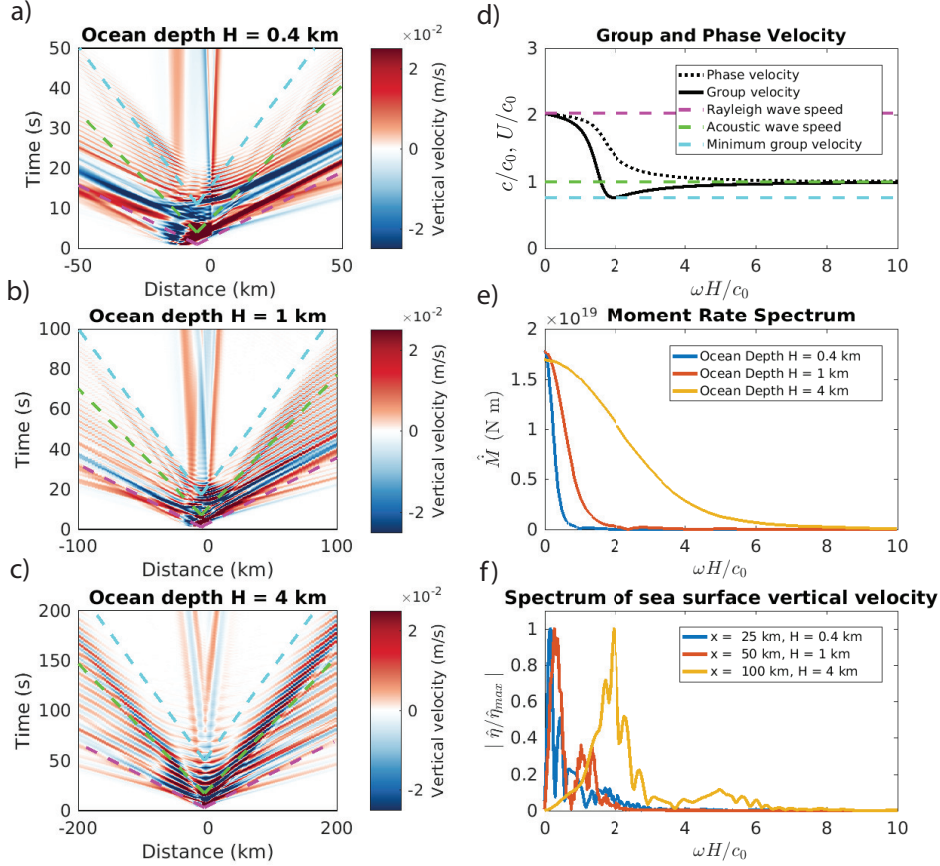


Figure 12. Same as Fig. 10 except for  $H = 1$  km.

727 spectrum, together with the ocean depth, determines the expression of the oceanic Rayleigh  
 728 wave mode that dominates the seismic/acoustic wavefield.

729 The results shown here help explain features in previous dynamic rupture simu-  
 730 lations and in observations. Simulations of the 2011 Tohoku-Oki earthquake by Kozdon  
 731 and Dunham (2014) revealed a complex wavefield within the ocean, as might be recorded



**Figure 13.** Space-time plots of sea surface vertical velocity showing oceanic Rayleigh waves for ocean depths  $H = 0.4$  km (a),  $H = 1$  km (b), and  $H = 4$  km (c) using the fully-coupled method 4. Note different axes limits in (a), (b), and (c). (d) Phase ( $c$ ) and group velocity ( $U$ ), normalized by the ocean sound speed  $c_0$  for the oceanic Rayleigh wave mode. (e) Moment rate spectrum of dynamic rupture source. (f) Spectrum of vertical velocity on the sea surface, normalized by maximum amplitude to facilitate comparison.

732 by ocean bottom seismometers and/or pressure sensors. The oceanic Rayleigh wave is  
 733 a prominent feature in these simulations. The deep ocean in the Japan Trench (reach-  
 734 ing 7 km at the trench) leads to the expression of both normally and anomalously dis-  
 735 persed branches of the oceanic Rayleigh wave, with the largest amplitude waves propa-  
 736 gating slower than the ocean sound speed. Similar waveform features are seen in simu-  
 737 lations by Wilson and Ma (2021) using the structural model for Cascadia developed by  
 738 Lotto et al. (2018), despite the ocean only reaching about 3 km depth. Wilson and Ma  
 739 (2021) demonstrate how excitation of oceanic Rayleigh waves depends on shallow rup-  
 740 ture behavior, in particular whether or not rupture occurs via localized slip on the megath-  
 741 rust or transitions to distributed inelastic yielding of sediments.

742 Oceanic Rayleigh waves, which have long been recognized in seismology (Press et  
 743 al., 1950), have also been observed in both recorded data and 3D wave propagation simu-  
 744 lations. In their study of an earthquake offshore Japan, Nakamura et al. (2012) iden-  
 745 tify large amplitude arrivals in K-NET seismograms along the coast that they attribute

746 to the oceanic Rayleigh waves through 3D wave propagation simulations and dispersion  
747 analysis. Similar results were obtained by Sugioka et al. (2012) for very low frequency  
748 earthquakes offshore in the Nankai Trough. Todoriki et al. (2016) further confirmed this  
749 interpretation by performing more idealized simulations with uniform depth oceans in  
750 addition to modeling waveforms from two earthquakes offshore Japan. Their synthetic  
751 seismograms show the same water depth dependence that we have identified in our sim-  
752 ulations, with the anomalously dispersed branch and Airy phase being suppressed for  
753 sufficiently shallow water. Takemura et al. (2018) has extended this work by focusing  
754 on complexities created by the low velocity accretionary prism in the Nankai Trough,  
755 and Noguchi et al. (2016) have studied the conversion of oceanic Rayleigh waves to con-  
756 tinental Rayleigh waves as the waves approach land. While these studies utilized seis-  
757 mograms on land, other studies have identified similar dispersed waveform features in  
758 ambient noise Green’s functions from ocean bottom seismometer data (Takeo et al., 2014;  
759 Takagi et al., 2021).

## 760 8 Conclusion

761 In this study, we utilized the Lotto and Dunham (2015) method for coupled earth-  
762 quake and tsunami simulations, which was recently implemented in the 3D code Seis-  
763 Sol (Krenz et al., 2021). We verified this implementation by performing convergence tests  
764 against an analytical eigenmode solution in Appendix A. We then compared the fully  
765 coupled method (method 1) with two commonly used tsunami modeling methods (meth-  
766 ods 2 and 3) that utilize static or time-dependent seafloor displacement from a previ-  
767 ously conducted earthquake simulation. In addition, we investigated an additional method  
768 (method 4), introduced by Saito et al. (2019), that also involves separate earthquake and  
769 tsunami simulations but combines them to provide an approximation to the full seismic,  
770 acoustic, and tsunami wavefield. Starting from the governing equations for the fully cou-  
771 pled method, we showed how the other methods can be derived by employing various  
772 approximations. In particular, this establishes the formal basis for the superposition method  
773 4 and explains why it provides an accurate approximation of the fully coupled solution  
774 for most problems of interest in coupled earthquake-tsunami modeling. We also iden-  
775 tified dimensionless parameters that can be used to determine if the assumption under-  
776 lying one of the approximate methods is justified and we provided numerical simulations  
777 to support our analysis. To compare the methods, we first studied the ocean response  
778 to an imposed seafloor displacement. This was done analytically, using seafloor-to-sea  
779 surface transfer functions that quantify how seafloor uplift excites different wave modes  
780 within the ocean, and using numerical simulations. We then extended the comparison  
781 to a dynamic rupture model with an elastic solid underlying the ocean. The presence  
782 of the elastic solid alters the structure and dispersion properties of wave modes in the  
783 system. The first acoustic mode in the rigid-bottomed case, which exists only above a  
784 cut-off frequency, becomes an oceanic Rayleigh wave that exists at all frequencies. The  
785 dispersion properties of the oceanic Rayleigh wave, together with the source spectrum,  
786 control the wavefield expression of the earthquake source. Our work can help guide fu-  
787 ture modeling and data interpretation efforts for offshore earthquakes and tsunamis, es-  
788 pecially when working with data from ocean-bottom instruments.

789

## Appendix A Verification of 3D fully-coupled method

790

791

792

793

794

In this appendix, we present a computational verification test to ensure the correct implementation of the modified free surface boundary condition with gravity in the 3D code SeisSol. To do this, we compare the numerical solution against analytical eigenmode solutions for the ocean response, obtained by extending the 2D solution of Lotto and Dunham (2015) and Wilson and Ma (2021) to 3D.

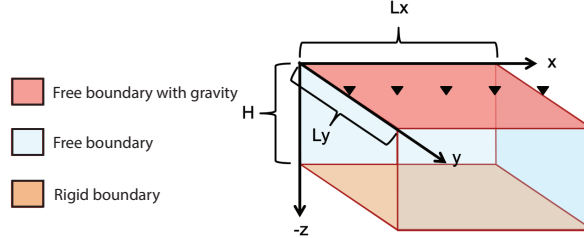


**Figure A1.** Eigenmode problem used for verification.

The eigenmode solution is obtained for a compressible ocean in the shape of a cuboid of height  $H$  and horizontal widths  $L_x$  and  $L_y$  (Fig. A1). The pressure is set to zero on the sides, the bottom is rigid ( $v_z = 0$ ), and on the top we enforce equations (6) and (7). Using standard techniques for solving linear, constant coefficient differential equations (e.g., Aki & Richards, 2002), we seek a standing wave solution to the homogeneous equations (2)-(5) and boundary conditions with horizontal wavenumbers  $k_x$  and  $k_y$  and angular frequency  $\omega$ . The solution, which can also be obtained via rotation of the 2D Lotto and Dunham (2015) solution about the  $z$  axis, is

$$p(x, y, z, t) = \sin(k_x x) \sin(k_y y) \sin(\omega t) \left( \sinh(k^* z) + g \frac{k^*}{\omega^2} \cosh(k^* z) \right), \quad (\text{A1})$$

$$v_x(x, y, z, t) = \frac{k_x}{\omega \rho} \cos(k_x x) \sin(k_y y) \cos(\omega t) \left( \sinh(k^* z) + g \frac{k^*}{\omega^2} \cosh(k^* z) \right), \quad (\text{A2})$$

$$v_y(x, y, z, t) = \frac{k_y}{\omega \rho} \sin(k_x x) \cos(k_y y) \cos(\omega t) \left( \sinh(k^* z) + g \frac{k^*}{\omega^2} \cosh(k^* z) \right), \quad (\text{A3})$$

$$v_z(x, y, z, t) = \frac{k^*}{\omega \rho} \sin(k_x x) \sin(k_y y) \cos(\omega t) \left( \cosh(k^* z) + g \frac{k^*}{\omega^2} \sinh(k^* z) \right), \quad (\text{A4})$$

and

$$\eta(x, y, t) = \frac{k^*}{\omega^2 \rho} \sin(k_x x) \sin(k_y y) \sin(\omega t), \quad (\text{A5})$$

with

$$k^* = \sqrt{k_x^2 + k_y^2 - \frac{\omega^2}{c^2}}. \quad (\text{A6})$$

The dispersion relation

$$\omega^2 = g k^* \tanh(k^* H) \quad (\text{A7})$$

relates angular frequency and wavenumbers. The finite horizontal extent of the ocean, with pressure vanishing on the sides, leads to a discrete spectrum for the horizontal wavenumbers:

$$k_x = m_x \pi / L_x, \quad m_x = 0, 1, \dots; \quad k_y = m_y \pi / L_y, \quad m_y = 0, 1, \dots \quad (\text{A8})$$

795

796

797

Next, we use this analytical eigenmode solution to set the initial pressure, particle velocities, and sea surface height in a numerical simulation. We select  $L_x = L_y = 10$  km,  $H = 1$  km, and  $m_x = m_y = 1$ ;  $\rho$ ,  $c$ , and  $g$  are the same as in Table 2. Then

798 we solve the dispersion relation (A7) for  $\omega$ . There is an infinite number of solutions, which  
 799 we index by  $n$ , with  $n = 0$  being the surface gravity wave mode and  $n = 1, 2, \dots$  be-  
 800 ing the acoustic modes. Here we show results for  $n = 0, 1$ , and 2.

801 The domain is 10 km by 10 km in the horizontal direction with depth  $H = 1$  km.  
 802 For the base refinement the domain is divided into 100 (10 by 10) equal-sized boxes with  
 803 6 hexahedral elements per box. Therefore, the domain's base level of resolution has 600  
 804 equally-sized elements. We refine (in each direction and in time) by a factor of 2, 4, 8,  
 805 16, and 32 for each higher refinement level. Each successive refinement level therefore  
 806 has  $2^3 = 8$  times more elements than the previous refinement level. We evaluate poly-  
 807 nomial orders 2, 4, and 6 within each element. The problem runs for one oscillation peri-  
 808 od (i.e., to final time  $t = 2\pi/\omega$ ). We compute the  $L_2$  norm of the error in pressure  
 809 over the 3D domain at this final time. Fig. A2 and Tables A1–A3 show the results. The  
 810 calculated convergence rates match the expected order of accuracy except at extremely  
 811 high refinement levels for the high order cases, which we speculate is due to the onset  
 812 of roundoff error.

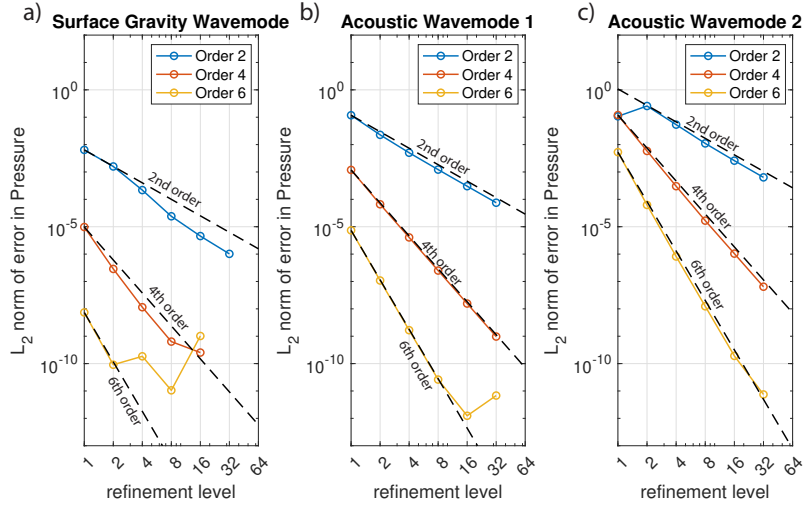


Figure A2. Convergence results for eigenmode verification study.

### Acknowledgments

813 L.S.A. was supported by National Science Foundation Graduate Research Fellowship DGE-  
 814 1656518, Stanford's Enhancing Diversity in Graduate Education (EDGE) Doctoral Fel-  
 815 lowship Program and Diversifying Academia, and Recruiting Excellence (DARE) Doc-  
 816 toral Fellowship Program. L.K. and A.-A.G. acknowledge funding from the European  
 817 Union's Horizon 2020 Research and Innovation Programme under grant agreement No.  
 818 823844 (ChEESSE – Centre of Excellence in Solid Earth) and the German Research Foun-  
 819 dation (DFG) project BA3529/6-1;GA2465/3-1 (CoCoReCS). A.-A.G. was supported  
 820 by the European Union's Horizon 2020 research and innovation programme under ERC  
 821 Starting grant no. 852992 (TEAR) and the National Science Foundation (NSF) project  
 822 EAR-2121666. The authors gratefully acknowledge the Gauss Centre for Supercomput-  
 823 ing e.V. ([www.gauss-centre.eu](http://www.gauss-centre.eu)) for providing computing time on the GCS Supercom-  
 824 puter SuperMUC-NG at Leibniz Supercomputing Centre ([www.lrz.de](http://www.lrz.de), through project  
 825 pn68fi).  
 826

827 Numerical simulations were performed using SeisSol ([https://github.com/SeisSol/](https://github.com/SeisSol/SeisSol.git)  
 828 [SeisSol.git](https://github.com/SeisSol/SeisSol.git)) for 3D fully-coupled simulations, FDMAP (<https://bitbucket.org/ericmdunham/>

**Table A1.** Gravity wave mode ( $n = 0$ ) convergence rate table

Mode 0	Order 2		Order 4		Order 6	
Refinement Level	Error	Rate	Error	Rate	Error	Rate
1	6.4079e-03		9.7417e-06		7.3848e-09	
2	1.5877e-03	2.0129	2.8730e-07	5.0835	9.0906e-11	6.3440
4	2.1795e-04	2.8649	1.1462e-08	4.6476	1.8458e-10	-1.0218
8	2.4062e-05	3.1792	6.3695e-10	4.1696	1.0562e-11	4.1273
16	4.5579e-06	2.4003	2.5302e-10	1.3319	1.0187e-09	-6.5917
32	1.0200e-06	2.1599	_*	_*	_*	_*

\* Not run due to computational expense.

**Table A2.** Acoustic wave mode ( $n = 1$ ) convergence rate table

Mode 1	Order 2		Order 4		Order 6	
Refinement Level	Error	Rate	Error	Rate	Error	Rate
1	1.1800e-01		1.1889e-03		7.3651e-06	
2	2.2707e-02	2.3776	6.6027e-05	4.1704	1.0851e-07	6.0848
4	5.0400e-03	2.1716	4.0673e-06	4.0209	1.6614e-09	6.0293
8	1.2196e-03	2.047	2.5038e-07	4.0219	2.6089e-11	5.9928
16	3.0241e-04	2.0118	1.5616e-08	4.003	1.2432e-12	4.3914
32	7.5284e-05	2.0061	9.7317e-10	4.0042	6.8058e-12	-2.4528

**Table A3.** Acoustic wave mode ( $n = 2$ ) convergence rate table

Mode 2	Order 2		Order 4		Order 6	
Refinement Level	Error	Rate	Error	Rate	Error	Rate
1	1.0791e-01		1.1970e-01		5.3067e-03	
2	2.5684e-01	-1.2511	5.8573e-03	4.353	6.2510e-05	6.4076
4	5.3644e-02	2.2594	3.0234e-04	4.276	8.1661e-07	6.2583
8	1.1045e-02	2.28	1.6683e-05	4.1797	1.2381e-08	6.0434
16	2.588e-03	2.0936	1.0406e-06	4.0029	1.9104e-10	6.0181
32	6.3474e-04	2.0276	6.4365e-08	4.015	7.4649e-12	4.6776



829 `fdmap`) for 2D linear long wave simulations, and the code developed by Saito et al. (2010);  
 830 Saito (2019) for 2D Boussinesq simulations. Simulation setup files and documentation  
 831 are available at DOI:10.25740/jv404dc0795 (<https://pur1.stanford.edu/jv404dc0795>).

## 832 References

- 833 Aki, K., & Richards, P. (2002). *Quantitative seismology*. University Science Books.
- 834 Amlani, F., Bhat, H. S., Simons, W. J., Schubnel, A., Vigny, C., Rosakis, A. J., ...  
 835 Abidin, H. Z. (2022). Supershear shock front contribution to the tsunami from  
 836 the 2018 Mw 7.5 Palu, Indonesia earthquake. *Geophysical Journal Interna-*  
 837 *tional*, *230*(3), 2089–2097.
- 838 Aniko Wirp, S., Gabriel, A.-A., Schmeller, M., H Madden, E., van Zelst, I., Krenz,  
 839 L., ... Rannabauer, L. (2021). 3D linked subduction, dynamic rupture,  
 840 tsunami, and inundation modeling: Dynamic effects of supershear and tsunami  
 841 earthquakes, hypocenter location, and shallow fault slip. *Frontiers in Earth*  
 842 *Science*, *9*, 177.
- 843 Baba, T., Allgeyer, S., Hossen, J., Cummins, P. R., Tsushima, H., Imai, K., ...  
 844 Kato, T. (2017). Accurate numerical simulation of the far-field tsunami caused  
 845 by the 2011 Tohoku earthquake, including the effects of Boussinesq disper-  
 846 sion, seawater density stratification, elastic loading, and gravitational potential  
 847 change. *Ocean Modelling*, *111*, 46–54.
- 848 Baba, T., Ando, K., Matsuoka, D., Hyodo, M., Hori, T., Takahashi, N., ... oth-  
 849 ers (2016). Large-scale, high-speed tsunami prediction for the Great Nankai  
 850 Trough Earthquake on the K computer. *The International Journal of High*  
 851 *Performance Computing Applications*, *30*(1), 71–84.
- 852 Baba, T., Takahashi, N., Kaneda, Y., Ando, K., Matsuoka, D., & Kato, T. (2015).  
 853 Parallel implementation of dispersive tsunami wave modeling with a nesting al-  
 854 gorithm for the 2011 Tohoku tsunami. *Pure and Applied Geophysics*, *172*(12),  
 855 3455–3472.
- 856 Bernard, E., & Titov, V. (2015). Evolution of tsunami warning systems and prod-  
 857 ucts. *Philosophical Transactions of the Royal Society A: Mathematical, Physi-*  
 858 *cal and Engineering Sciences*, *373*(2053), 20140371.
- 859 Biot, M. A. (1952). The interaction of Rayleigh and Stoneley waves in the ocean  
 860 bottom. *Bulletin of the Seismological Society of America*, *42*(1), 81–93.
- 861 Breuer, A., Heinecke, A., Rannabauer, L., & Bader, M. (2015). High-order ADER-  
 862 DG minimizes energy- and time-to-solution of seissol. In J. M. Kunkel &  
 863 T. Ludwig (Eds.), *High performance computing* (pp. 340–357). Cham: Springer  
 864 International Publishing.
- 865 Cheung, K. F., Lay, T., Sun, L., & Yamazaki, Y. (2022). Tsunami size variability  
 866 with rupture depth. *Nature Geoscience*, *15*(1), 33–36.
- 867 Comer, R. P. (1984). Tsunami generation: a comparison of traditional and normal  
 868 mode approaches. *Geophysical Journal International*, *77*(1), 29–41.
- 869 Dahlen, F., & Tromp, J. (1999). *Theoretical global seismology*. Princeton University  
 870 Press.
- 871 Duffy, D. G. (1992). On the generation of oceanic surface waves by underwater vol-  
 872 canic explosions. *Journal of volcanology and geothermal research*, *50*(3), 323–  
 873 344.
- 874 Dumbser, M., & Käser, M. (2006). An arbitrary high-order discontinuous Galerkin  
 875 method for elastic waves on unstructured meshes—II. The three-dimensional  
 876 isotropic case. *Geophysical Journal International*, *167*(1), 319–336.
- 877 Dunham, E. M., Belanger, D., Cong, L., & Kozdon, J. E. (2011). Earthquake  
 878 ruptures with strongly rate-weakening friction and off-fault plasticity, part  
 879 1: Planar faults. *Bulletin of the Seismological Society of America*, *101*(5),  
 880 2296–2307.
- 881 Elbanna, A., Abdelmeguid, M., Ma, X., Amlani, F., Bhat, H. S., Synolakis, C., &

- 882 Rosakis, A. J. (2021). Anatomy of strike-slip fault tsunami genesis. *Proceed-*  
 883 *ings of the National Academy of Sciences*, 118(19), e2025632118.
- 884 Eyov, E., Klar, A., Kadri, U., & Stiassnie, M. (2013). Progressive waves in a  
 885 compressible-ocean with an elastic bottom. *Wave Motion*, 50(5), 929–939.
- 886 Fujii, Y., & Satake, K. (2007). Tsunami source of the 2004 Sumatra–Andaman  
 887 earthquake inferred from tide gauge and satellite data. *Bulletin of the Seismo-*  
 888 *logical Society of America*, 97(1A), S192–S207.
- 889 Goda, K., Petrone, C., De Risi, R., & Rossetto, T. (2017). Stochastic coupled sim-  
 890 ulation of strong motion and tsunami for the 2011 tohoku, japan earthquake.  
 891 *Stochastic Environmental Research and Risk Assessment*, 31(9), 2337–2355.
- 892 Grezio, A., Babeyko, A., Baptista, M. A., Behrens, J., Costa, A., Davies, G., ...  
 893 others (2017). Probabilistic tsunami hazard analysis: Multiple sources and  
 894 global applications. *Reviews of Geophysics*, 55(4), 1158–1198.
- 895 Harris, R. A., Barall, M., Aagaard, B., Ma, S., Roten, D., Olsen, K., ... others  
 896 (2018). A suite of exercises for verifying dynamic earthquake rupture codes.  
 897 *Seismological Research Letters*, 89(3), 1146–1162.
- 898 Harris, R. A., Barall, M., Andrews, D. J., Duan, B., Ma, S., Dunham, E. M., ...  
 899 others (2011). Verifying a computational method for predicting extreme  
 900 ground motion. *Seismological Research Letters*, 82(5), 638–644.
- 901 Hayes, G. P., McNamara, D. E., Seidman, L., & Roger, J. (2014). Quantifying po-  
 902 tential earthquake and tsunami hazard in the lesser antilles subduction zone of  
 903 the caribbean region. *Geophysical Journal International*, 196(1), 510–521.
- 904 Kajiuura, K. (1963). The leading wave of a tsunami. *Bulletin of the Earthquake Re-*  
 905 *search Institute, University of Tokyo*, 41(3), 535–571.
- 906 Kajiuura, K. (1970). Tsunami source, energy and the directivity of wave radiation.  
 907 *Bulletin of the Earthquake Research Institute*, 48, 835–869.
- 908 Kawaguchi, K., Kaneda, Y., & Araki, E. (2008). The DONET: A real-time seafloor  
 909 research infrastructure for the precise earthquake and tsunami monitoring. In  
 910 *Oceans 2008-mts/ieec kobe techno-ocean* (pp. 1–4).
- 911 Kervella, Y., Dutykh, D., & Dias, F. (2007). Comparison between three-dimensional  
 912 linear and nonlinear tsunami generation models. *Theoretical and computational*  
 913 *fluid dynamics*, 21(4), 245–269.
- 914 Kozdon, J. E., & Dunham, E. M. (2013). Rupture to the trench: Dynamic rupture  
 915 simulations of the 11 march 2011 tohoku earthquake. *Bulletin of the Seismo-*  
 916 *logical Society of America*, 103(2B), 1275–1289.
- 917 Kozdon, J. E., & Dunham, E. M. (2014). Constraining shallow slip and tsunami  
 918 excitation in megathrust ruptures using seismic and ocean acoustic waves  
 919 recorded on ocean-bottom sensor networks. *Earth and Planetary Science*  
 920 *Letters*, 396, 56–65.
- 921 Kozdon, J. E., Dunham, E. M., & Nordström, J. (2012). Interaction of waves with  
 922 frictional interfaces using summation-by-parts difference operators: Weak en-  
 923 forcement of nonlinear boundary conditions. *Journal of Scientific Computing*,  
 924 50(2), 341–367.
- 925 Kozdon, J. E., Dunham, E. M., & Nordström, J. (2013). Simulation of dynamic  
 926 earthquake ruptures in complex geometries using high-order finite difference  
 927 methods. *Journal of Scientific Computing*, 55(1), 92–124.
- 928 Krenz, L., Uphoff, C., Ulrich, T., Gabriel, A.-A., Abrahams, L. S., Dunham, E. M.,  
 929 & Bader, M. (2021). 3D acoustic-elastic coupling with gravity: the dynam-  
 930 ics of the 2018 Palu, Sulawesi earthquake and tsunami. In *Proceedings of the*  
 931 *international conference for high performance computing, networking, storage*  
 932 *and analysis* (pp. 1–14).
- 933 Kubota, T., Saito, T., Fukao, Y., Sugioka, H., Ito, A., Tonegawa, T., ... Yamashita,  
 934 M. (2021). Earthquake rupture and tsunami generation of the 2015 Mw 5.9  
 935 Bonin event revealed by in situ pressure gauge array observations and inte-  
 936 grated seismic and tsunami wave simulation. *Geophysical Research Letters*,

- 48(22), e2021GL095915.
- 937 Lay, T., Yamazaki, Y., Ammon, C. J., Cheung, K. F., & Kanamori, H. (2011).  
 938 The 2011 Mw 9.0 off the Pacific coast of Tohoku earthquake: Comparison of  
 939 deep-water tsunami signals with finite-fault rupture model predictions. *Earth,*  
 940 *planets and space*, *63*(7), 797–801.
- 942 LeVeque, R. J., Waagan, K., González, F. I., Rim, D., & Lin, G. (2016). Generat-  
 943 ing random earthquake events for probabilistic tsunami hazard assessment. In  
 944 *Global tsunami science: Past and future, volume i* (pp. 3671–3692). Springer.
- 945 Levin, B. W., Nosov, M., et al. (2009). *Physics of tsunamis* (Vol. 327). Springer.
- 946 Lindsey, N. J., Dawe, T. C., & Ajo-Franklin, J. B. (2019). Illuminating seafloor  
 947 faults and ocean dynamics with dark fiber distributed acoustic sensing. *Sci-*  
 948 *ence*, *366*(6469), 1103–1107.
- 949 Liu, P. L.-F., Wang, X., & Salisbury, A. J. (2009). Tsunami hazard and early warn-  
 950 ing system in South China Sea. *Journal of Asian Earth Sciences*, *36*(1), 2–12.
- 951 Lotto, G. C., & Dunham, E. M. (2015). High-order finite difference modeling of  
 952 tsunami generation in a compressible ocean from offshore earthquakes. *Compu-*  
 953 *tational Geosciences*, *19*(2), 327–340. doi: 10.1007/s10596-015-9472-0
- 954 Lotto, G. C., Jeppson, T. N., & Dunham, E. M. (2018). *Fully Coupled Simulations*  
 955 *of Megathrust Earthquakes and Tsunamis in the Japan Trench, Nankai Trough,*  
 956 *and Cascadia Subduction Zone*. doi: 10.1007/s00024-018-1990-y
- 957 Lotto, G. C., Nava, G., & Dunham, E. M. (2017). Should tsunami simulations in-  
 958 clude a nonzero initial horizontal velocity? *Earth, Planets and Space*, *69*(1).  
 959 doi: 10.1186/s40623-017-0701-8
- 960 Madden, E. H., Bader, M., Behrens, J., van Dinther, Y., Gabriel, A.-A.,  
 961 Rannabauer, L., ... van Zelst, I. (2021). Linked 3-D modelling of megathrust  
 962 earthquake-tsunami events: from subduction to tsunami run up. *Geophysical*  
 963 *Journal International*, *224*(1), 487–516.
- 964 Maeda, T., & Furumura, T. (2013). FDM simulation of seismic waves, ocean acous-  
 965 tic waves, and tsunamis based on tsunami-coupled equations of motion. *Pure*  
 966 *and Applied Geophysics*, *170*(1-2), 109–127.
- 967 Matsumoto, H., Nosov, M. A., Kolesov, S. V., & Kaneda, Y. (2017). Analysis of  
 968 pressure and acceleration signals from the 2011 Tohoku earthquake observed  
 969 by the DONET seafloor network. *Journal of Disaster Research*, *12*(1), 163–  
 970 175.
- 971 Mulia, I. E., Heidarzadeh, M., & Satake, K. (2022). Effects of depth of fault slip  
 972 and continental shelf geometry on the generation of anomalously long-period  
 973 tsunami by the July 2020 Mw 7.8 Shumagin (Alaska) earthquake. *Geophysical*  
 974 *Research Letters*, *49*(3), e2021GL094937.
- 975 Nakamura, T., Takenaka, H., Okamoto, T., & Kaneda, Y. (2012). Fdm simulation  
 976 of seismic-wave propagation for an aftershock of the 2009 suruga bay earth-  
 977 quake: effects of ocean-bottom topography and seawater layer. *Bulletin of the*  
 978 *Seismological Society of America*, *102*(6), 2420–2435.
- 979 Noguchi, S., Maeda, T., & Furumura, T. (2016). Ocean-influenced Rayleigh waves  
 980 from outer-rise earthquakes and their effects on durations of long-period  
 981 ground motion. *Geophysical Journal International*, *205*(2), 1099–1107.
- 982 Nosov, M. (1999). Tsunami generation in compressible ocean. *Physics and Chem-*  
 983 *istry of the Earth, Part B: Hydrology, Oceans and Atmosphere*, *24*(5), 437–  
 984 441.
- 985 Nosov, M., & Kolesov, S. (2007). Elastic oscillations of water column in the 2003  
 986 Tokachi-oki tsunami source: in-situ measurements and 3-D numerical mod-  
 987 elling. *Natural Hazards and Earth System Sciences*, *7*(2), 243–249.
- 988 Nosov, M. A., & Kolesov, S. V. (2011). Optimal initial conditions for simulation of  
 989 seismotectonic tsunamis. *Pure and Applied Geophysics*, *168*(6), 1223–1237.
- 990 Okada, Y. (1985). Surface deformation due to shear and tensile faults in a half-  
 991 space. *Bulletin of the seismological society of America*, *75*(4), 1135–1154.

- 992 Pelties, C., Gabriel, A. A., & Ampuero, J. P. (2014). Verification of an ADER-DG  
993 method for complex dynamic rupture problems. *Geoscientific Model Develop-*  
994 *ment*. doi: 10.5194/gmd-7-847-2014
- 995 Press, F., Ewing, M., & Tolstoy, I. (1950). The airy phase of shallow-focus subma-  
996 rine earthquakes. *Bulletin of the Seismological Society of America*, 40(2), 111–  
997 148.
- 998 Saito, T. (2019). Tsunami generation and propagation. In (chap. 5, Tsunami Gener-  
999 ation). Springer.
- 1000 Saito, T., Baba, T., Inazu, D., Takemura, S., & Fukuyama, E. (2019). Synthe-  
1001 sizing sea surface height change including seismic waves and tsunami using a  
1002 dynamic rupture scenario of anticipated nankai trough earthquakes. *Tectono-*  
1003 *physics*, 769, 228166.
- 1004 Saito, T., & Furumura, T. (2009). Three-dimensional tsunami generation simula-  
1005 tion due to sea-bottom deformation and its interpretation based on the linear  
1006 theory. *Geophysical Journal International*, 178(2), 877–888.
- 1007 Saito, T., & Kubota, T. (2020). Tsunami modeling for the deep sea and inside focal  
1008 areas. *Annual Review of Earth and Planetary Sciences*, 48, 121–145.
- 1009 Saito, T., Satake, K., & Furumura, T. (2010). Tsunami waveform inversion includ-  
1010 ing dispersive waves: the 2004 earthquake off Kii Peninsula, Japan. *Journal of*  
1011 *Geophysical Research: Solid Earth*, 115(B6).
- 1012 Saito, T., & Tsushima, H. (2016a). Synthesizing ocean bottom pressure records  
1013 including seismic wave and tsunami contributions: Toward realistic tests of  
1014 monitoring systems. *Journal of Geophysical Research: Solid Earth*, 121(11),  
1015 8175–8195.
- 1016 Saito, T., & Tsushima, H. (2016b). Synthesizing ocean bottom pressure records  
1017 including seismic wave and tsunami contributions: Toward realistic tests of  
1018 monitoring systems. *Journal of Geophysical Research: Solid Earth*. doi:  
1019 10.1002/2016JB013195
- 1020 Satake, K., Fujii, Y., Harada, T., & Namegaya, Y. (2013). Time and space distribu-  
1021 tion of coseismic slip of the 2011 Tohoku earthquake as inferred from tsunami  
1022 waveform data. *Bulletin of the seismological society of America*, 103(2B),  
1023 1473–1492.
- 1024 Scala, A., Lorito, S., Romano, F., Murphy, S., Selva, J., Basili, R., . . . others (2020).  
1025 Effect of shallow slip amplification uncertainty on probabilistic tsunami hazard  
1026 analysis in subduction zones: use of long-term balanced stochastic slip models.  
1027 *Pure and Applied Geophysics*, 177(3), 1497–1520.
- 1028 Sells, C. L. (1965). The effect of a sudden change of shape of the bottom of a  
1029 slightly compressible ocean. *Philosophical Transactions of the Royal Society of*  
1030 *London. Series A, Mathematical and Physical Sciences*, 258(1092), 495–528.
- 1031 Selva, J., Lorito, S., Volpe, M., Romano, F., Tonini, R., Perfetti, P., . . . others  
1032 (2021). Probabilistic tsunami forecasting for early warning. *Nature communi-*  
1033 *cations*, 12(1), 1–14.
- 1034 Simons, M., Minson, S. E., Sladen, A., Ortega, F., Jiang, J., Owen, S. E., . . . oth-  
1035 ers (2011). The 2011 magnitude 9.0 Tohoku-Oki earthquake: Mosaicking the  
1036 megathrust from seconds to centuries. *science*, 332(6036), 1421–1425.
- 1037 Sladen, A., Rivet, D., Ampuero, J. P., De Barros, L., Hello, Y., Calbris, G., &  
1038 Lamare, P. (2019). Distributed sensing of earthquakes and ocean-solid Earth  
1039 interactions on seafloor telecom cables. *Nature communications*, 10(1), 1–8.
- 1040 Song, Y. T., Fu, L. L., Zlotnicki, V., Ji, C., Hjorleifsdottir, V., Shum, C. K., &  
1041 Yi, Y. (2008). The role of horizontal impulses of the faulting continental  
1042 slope in generating the 26 December 2004 tsunami. *Ocean Modelling*. doi:  
1043 10.1016/j.ocemod.2007.10.007
- 1044 Song, Y. T., & Han, S.-C. (2011). Satellite Observations Defying the Long-Held  
1045 Tsunami Genesis Theory. In *Remote sensing of the changing oceans*. doi: 10  
1046 .1007/978-3-642-16541-2\_17

- 1047 Song, Y. T., Mohtat, A., & Yim, S. C. (2017). New insights on tsunami genesis and  
1048 energy source. *Journal of Geophysical Research: Oceans*, *122*(5), 4238–4256.
- 1049 Stoneley, R. (1926). The effect of the ocean on Rayleigh waves. *Geophysical Sup-*  
1050 *plements to the Monthly Notices of the Royal Astronomical Society*, *1*(7),  
1051 349–356.
- 1052 Sugioka, H., Okamoto, T., Nakamura, T., Ishihara, Y., Ito, A., Obana, K., ...  
1053 Fukao, Y. (2012). Tsunamigenic potential of the shallow subduction plate  
1054 boundary inferred from slow seismic slip. *Nature Geoscience*, *5*(6), 414–418.
- 1055 Takagi, R., Toyokuni, G., & Chikasada, N. (2021). Ambient noise correlation anal-  
1056 ysis of s-net records: extracting surface wave signals below instrument noise  
1057 levels. *Geophysical Journal International*, *224*(3), 1640–1657.
- 1058 Takemura, S., Kimura, T., Saito, T., Kubo, H., & Shiomi, K. (2018). Moment tensor  
1059 inversion of the 2016 southeast offshore mie earthquake in the tonankai region  
1060 using a three-dimensional velocity structure model: effects of the accretionary  
1061 prism and subducting oceanic plate. *Earth, Planets and Space*, *70*(1), 1–19.
- 1062 Takeo, A., Forsyth, D. W., Weeraratne, D. S., & Nishida, K. (2014). Estimation of  
1063 azimuthal anisotropy in the NW Pacific from seismic ambient noise in seafloor  
1064 records. *Geophysical Journal International*, *199*(1), 11–22.
- 1065 Tanioka, Y., & Sataka, K. (1996). Fault parameters of the 1896 Sanriku tsunami  
1066 earthquake estimated from tsunami numerical modeling. *Geophysical Research*  
1067 *Letters*, *23*(13), 1549–1552.
- 1068 Tanioka, Y., & Satake, K. (1996). Tsunami generation by horizontal displacement of  
1069 ocean bottom. *Geophysical Research Letters*. doi: 10.1029/96GL00736
- 1070 Tanioka, Y., & Seno, T. (2001). Sediment effect on tsunami generation of the 1896  
1071 Sanriku tsunami earthquake. *Geophysical Research Letters*, *28*(17), 3389–  
1072 3392.
- 1073 Todoriki, M., Furumura, T., & Maeda, T. (2016). Effects of seawater on elongated  
1074 duration of ground motion as well as variation in its amplitude for offshore  
1075 earthquakes. *Geophysical Journal International*, ggw388.
- 1076 Tsushima, H., Hino, R., Tanioka, Y., Imamura, F., & Fujimoto, H. (2012). Tsunami  
1077 waveform inversion incorporating permanent seafloor deformation and its ap-  
1078 plication to tsunami forecasting. *Journal of Geophysical Research: Solid Earth*,  
1079 *117*(B3).
- 1080 Ulrich, T., Vater, S., Madden, E. H., Behrens, J., van Dinther, Y., Van Zelst, I., ...  
1081 Gabriel, A.-A. (2019). Coupled, physics-based modeling reveals earthquake dis-  
1082 placements are critical to the 2018 Palu, Sulawesi tsunami. *Pure and Applied*  
1083 *Geophysics*, *176*(10), 4069–4109.
- 1084 Uphoff, C., Rettenberger, S., Bader, M., Madden, E. H., Ulrich, T., Wollherr, S., &  
1085 Gabriel, A.-A. (2017). Extreme scale multi-physics simulations of the tsunami-  
1086 genic 2004 Sumatra megathrust earthquake. In *Proceedings of the international*  
1087 *conference for high performance computing, networking, storage and analysis*  
1088 (pp. 1–16).
- 1089 Ward, S. N. (1980). Relationships of tsunami generation and an earthquake source.  
1090 *Journal of Physics of the Earth*, *28*(5), 441–474.
- 1091 Ward, S. N. (1981). On tsunami nucleation: 1. A point source. *Journal of Geophys-  
1092 ical Research: Solid Earth*, *86*(B9), 7895–7900.
- 1093 Ward, S. N. (2001). *Tsunamis encyclopedia of physical science and technology ed r*  
1094 *meyers*. Amsterdam: Elsevier.
- 1095 Wilson, A., & Ma, S. (2021). Wedge plasticity and fully coupled simulations of dy-  
1096 namic rupture and tsunami in the cascadia subduction zone. *Journal of Geo-*  
1097 *physical Research: Solid Earth*, *126*(7), e2020JB021627.
- 1098 Witter, R. C., Zhang, Y. J., Wang, K., Priest, G. R., Goldfinger, C., Stimely, L., ...  
1099 Ferro, P. A. (2013). Simulated tsunami inundation for a range of Cascadia  
1100 megathrust earthquake scenarios at bandon, oregon, usa. *Geosphere*, *9*(6),  
1101 1783–1803.

- 1102 Yamamoto, N., Hirata, K., Aoi, S., Suzuki, W., Nakamura, H., & Kunugi, T. (2016).  
1103 Rapid estimation of tsunami source centroid location using a dense offshore  
1104 observation network. *Geophysical Research Letters*, *43*(9), 4263–4269.
- 1105 Yamazaki, Y., Cheung, K. F., & Lay, T. (2018). A self-consistent fault slip model for  
1106 the 2011 Tohoku earthquake and tsunami. *Journal of Geophysical Research:*  
1107 *Solid Earth*, *123*(2), 1435–1458.
- 1108 Yokota, Y., Koketsu, K., Fujii, Y., Satake, K., Sakai, S., Shinohara, M., &  
1109 Kanazawa, T. (2011). Joint inversion of strong motion, teleseismic, geodetic,  
1110 and tsunami datasets for the rupture process of the 2011 Tohoku earthquake.  
1111 *Geophysical Research Letters*, *38*(7).
- 1112 Zhan, Z., Cantono, M., Kamalov, V., Mecozzi, A., Müller, R., Yin, S., & Castel-  
1113 lanos, J. C. (2021). Optical polarization-based seismic and water wave sensing  
1114 on transoceanic cables. *Science*, *371*(6532), 931–936.